https://doi.org/10.5194/egusphere-2025-374
Preprint. Discussion started: 5 February 2025

A machine learning-based perspective on deep convective clouds and their organisation in 3D. Part I: Influence of deep convective cores on the cloud life-cycle

Sarah Brüning[1] and Holger Tost[1]

[1]Institute for Physics of the Atmosphere, Johannes Gutenberg University Mainz, Johann-Joachim-Becher-Weg 21, Mainz, 55128, Rhineland-Palatinate, Germany

Correspondence: Sarah Brüning (sbruenin@uni-mainz.de)

Abstract. In this two-part sequence of papers, we investigate spatio-temporal patterns of convective cloud activity and organisation. The analysis employs a machine learning (ML)-based contiguous 3D extrapolation of satellite data from multiple sensors to simultaneously follow horizontal and vertical cloud development. Our study covers West Africa, a hotspot for intense convection and severe weather. In this part, we derive seasonal and diurnal variations for convective cloud properties during spring (March–May) and summer (June–August). Moreover, we explore the connection between the number of deep convective cores (DCCs) and the cloud life-cycle. For that purpose, we track the evolution of convective systems and their core regions. More than 80 % of detected clouds contain a single convective core and persist between 1–3 hours. These isolated clouds have an enhanced absolute cooling but weaker anvil growth and updraft strength during their growth stage than clustered systems. The average difference between oceanic and continental cloud properties accounts for about 10 %. However, we detect a high seasonal variability and a surface-specific diurnal cycle. We find long-lasting cloud clusters with more intense core regions over continental Africa. Within these clusters, the interaction between cores may renew convective activity. The horizontal growth of convective clouds is about 5–10 % more intense over land in both seasons, even though convective activity over the ocean increases stronger in summer. While our results emphasise an enhanced convective activity over land, we suggest further analysis of regional patterns of clustered convection and their hydro-climatological impact.

1 Introduction

Convective clouds substantially impact the hydrological cycle of the Earth through their radiative forcing and feedback mechanisms (Roca et al., 2010). Research shows that clouds may enhance climate warming. However, they are still regarded as one of the largest sources of uncertainty for climate sensitivity studies (Chen et al., 2021). Moreover, convective clouds are major producers of severe weather (Kukulies et al., 2021; Haberlie and Ashley, 2018). Large-scale cloud clusters, like mesoscale convective systems (MCSs), are responsible for extreme weather events such as hail, strong winds, and extreme precipita-

https://doi.org/10.5194/egusphere-2025-374
Preprint. Discussion started: 5 February 2025

tion (Prein et al., 2024). Due to this threat for society and nature, an accurate representation of convective clouds remains of particular interest (Guillaume et al., 2018).

Houze Jr. (2004) defined a MCS as a convective storm complex with an axis length of 100 km and more. Typically, it consists of a contiguous cold cloud shield composed of one or more deep convective cores (DCCs), strong vertical updrafts that merge the cores at higher altitudes (Zipser and LeMone, 1980), and large anvils flowing out from the region of convective activity (Horner and Gryspeerdt, 2023). By counting the number of DCCs, we can approximate the degree of convective organisation. Higher numbers of DCCs come along with a stronger organisation, which, in turn, enhances the potential hazard of the cluster (Jones et al., 2024). For instance, DCCs are drivers of intense precipitation. In contrast, the stratiform anvil and cirrus canopy produce only lighter rain (Houze Jr., 2004). The size of a DCC ranges between 10 – 100 km with an average lifetime of up to 1–3 h, whereas the cloud anvil can persist up to 10–20 h or longer (Chen and Houze, 1997). We observe an idealised life-cycle that can be divided into three stages: the convective initiation (CI), the maturity phase (MAT), and the dissipation of the cloud (Fiolleau and Roca, 2013). Deep convective cells are triggered during the CI to bring the condensate upwards. In the maturity stage, the stratiform anvil and associated mesoscale circulation build up while deep convective cells still exist. In the dissipation stage, deep convection stops, and the cloud slowly fades out (Houze and Hobbs, 1982). The life-cycle of an MCS is connected to the location, daytime and surface type (Houze Jr., 2004). Small and medium-sized MCSs over land occur most frequently in the afternoon. This peak is associated with local thermal instability and (given the underlying surface properties potentially) a sea breeze circulation. Over the sea, we detect a weak semi-diurnal variability caused by the thermal properties of the underlying surface and the local circulation (Li et al., 2021). The structure and associated precipitation of MCSs differ with the region of genesis, e.g., when comparing the tropics and mid-latitudes (Kukulies et al., 2021).

Most of our understanding of convective clouds originates from observational data (Haynes et al., 2009). Remote sensing instruments provide highly-resolved data that help investigate the temporal evolution of MCSs (Bacmeister and Stephens, 2011), contributing towards a more realistic representation of cloud feedback mechanisms in climate models (Chen et al., 2021). Data from passive and active sensors are suitable for detecting convective clouds beginning from their CI (Mecikalski et al., 2010). For passive sensors, a combination of data in the infrared (IR) spectra can be used to understand cloud-top signatures. While they provide a detailed view of the horizontal evolution of the cloud (Jones et al., 2023), they lack information on the vertical cloud structure (Haberlie and Ashley, 2018). Relying only on infrared (IR) brightness temperatures as a proxy for convective activity can lead to a misclassification of cirrus or stratiform clouds as deep convection (Kukulies et al., 2021). In contrast, active sensors provide more detailed information on the vertical dimension (Bacmeister and Stephens, 2011). Previous studies by Bacmeister and Stephens (2011) or Oreopoulos et al. (2017) used the radar reflectivity from active sensors to detect the vertical structure of hydrometeors. Nevertheless, both sensor types derive data only from a 2D perspective or for a limited area. Following Masunaga and Luo (2016), global 3D observations could deepen the understanding of convective clouds. However, no operating satellite provides this seamless coverage of the cloud structure.

Convective cloud detection often consists of differentiating core regions from their surrounding background (Steiner et al., 1995). A convective feature is defined by a cold peak in its core region and an associated anvil with a warmer temperature (Fiolleau and Roca, 2013). Morphological characteristics, such as aspect ratio, length, width, and area, classify different types of convective systems (Ganetis et al., 2018). Clouds appear as moving phenomena due to diffusive, advective, dynamic, and thermodynamic processes (Sokolowsky et al., 2024). Early studies on their life-cycle often relied on manually identifying cloud movements (Masunaga and Luo, 2016). In recent years, the development of automated detection algorithms increased the amount of processed data significantly (e.g., Fiolleau and Roca (2013); Feng et al. (2023); Heikenfeld et al. (2019)). Most of these algorithms detect individual clouds or cloud clusters before linking the identified objects from one time step to the next (Prein et al., 2024).

Today, a variety of tools exist for cloud tracking. However, they are often limited to a specific use case. To account for the detection of convective cores and their corresponding anvil clouds, Fiolleau and Roca (2013) developed the *TOOCAN* algorithm, which works well with MCSs but shows less robust results for isolated DCCs (Sokolowsky et al., 2024). Single convective cells undergo a more rapid dynamic development over relatively short timescales compared to MCSs (Orlanski, 1975). They are typically tracked using data from active remote sensing sensors (Haberlie and Ashley, 2018). The pioneering work in this field is *TITAN*, developed by Dixon and Wiener (1993) and recently updated by Raut et al. (2021) as *TINT*. Feng et al. (2023) designed the *PyFLEXTRKR* framework to provide a more general approach to tracking any 2D atmospheric objects through time. Although it offers a high degree of flexibility, its application is limited to two spatial dimensions. Contrasting, the *tobac* package allows the analysis of a 4D time series (Heikenfeld et al., 2019). Data with a higher dimensionality may offer an in-depth perspective on convective systems and their feedback mechanisms (Prein et al., 2024; Patra and Kalapureddy, 2021).

Even though convective systems have been studied for decades, there is limited knowledge on the 3D characteristics of DCCs. Due to the absence of suitable 3D data, the impact of DCCs on the cloud life-cycle is predominantly derived from 2D observations or simulation data (Cui et al., 2021). While active and passive sensors provide versatile information on the horizontal and vertical cloud structure, the sensors are subject to a spatio-temporal sampling in either dimension (Masunaga and Luo, 2016; Taylor et al., 2017). To close the data availability gap, we use a machine learning (ML) framework to extrapolate contiguous 3D radar reflectivities from 2D sensors (Brüning et al., 2024). Our goal is to provide a detailed perspective of the combined horizontal and vertical evolution of convective clouds and their DCCs. For each time step of 15 min, we predict a 3D radar reflectivity field by combining high resolution geostationary satellite imagery and the vertical cross sections of a cloud profiling radar (CPR). The data is merged into a 4D time series. Afterwards, we employ the *tobac* package to identify convective cloud trajectories within the predicted cloud field. Our aim is to compare the temporal variability of convective cloud and core properties over land and sea. A particular interest lies in assessing the cloud life-cycle for different degrees of convective organisation.

We organise the article as follows. In Sect. 2, we present the data used in this study. Section 3 provides an overview of the approach used for tracking and filtering convective clouds. We focus on the identification of isolated convective cells and MCSs, including the detection of DCCs. Section 4 presents a statistical analysis of the results focusing on the diurnal and seasonal distribution of convective cloud and core characteristics. Section 5 discusses the current limitations of the study and modifications of cloud organisation over land and sea. Finally, Sect. 6 contains the summary and principal conclusions.

2 Data

The area of interest (AOI) covers a region in West Africa between between 30° N–30° S and 30° W–30° E. We exclude extra-tropical regions from the analysis due to their diverging convective development (Jones et al., 2024). The environmental conditions in the AOI favour the development of intense convective activity (Takahashi et al., 2023). Furthermore, its heterogeneous landscape promotes high spatio-temporal variations in the occurrence and intensity of convective activity. Clouds with high convective activity, like MCSs, still challenge forecasts and risk assessments (Jackson et al., 2022; Vondou, 2012). We use six months of data from March to August 2019 reflecting the northward shift of the Inter-Tropical Convergence Zone (ITCZ) and the onset of the West African monsoon (WAM). The WAM substantially influences the West African climate and induces a high proportion of the accumulated annual rainfall, leading to frequent convective activity (Andrews et al., 2024; Kniffka et al., 2019). Our goal is to investigate the seasonality of convective clouds during the rainy season in the spring and summer, particularly regarding the impact of DCCs on the cloud life-cycle (Nicholson, 2018).

For this study, we use data from the Spinning Enhanced Visible and Infrared Imager (SEVIRI) sensor onboard the Meteosat-11 (MSG) satellite (Schmetz et al., 2002). As MSG SEVIRI is centred above the Equator at 0° longitude, our AOI is close to the nadir of the sensor. It provides measurements for 12 channels in the visible, near-infrared, and thermal-infrared spectra. From these, 11 have a temporal resolution of 15 min and a spatial resolution of 3 km; one is a high-resolution visible channel with a nadir resolution of 1 km (Table 1). We apply a machine learning (ML) algorithm to predict a time series of 3D radar reflectivities from 2D satellite data described in Brüning et al. (2024). The validation data for the ML model display vertical cross-sections of the cloud radar reflectivity. These data originate from the 94-GHz cloud profiling radar (CPR) onboard the CloudSat polar-orbiting satellite. The CPR is an active sensor that emits radiation pulses toward the Earth to detect vertical profiles of cloud hydrometeors (Oreopoulos et al., 2017). It has a vertical resolution of 240 m with 125 bins and a horizontal resolution of 1.4 km across and 1.8 km along the track (Stephens et al., 2008). We train our model using radar reflectivities from the level-2 2B-GEOPROF product filtered by the cloud mask quality flag (Marchand et al., 2008).

To extract training samples, we apply a spatio-temporal matching scheme to the satellite data (Taylor et al., 2017). The output of this routine is fed into a Res-UNet, which was designed for a seamless segmentation of images of arbitrary size (Ronneberger et al., 2015). Our studies employs the Res-UNet to predict seamless 3D cloud reflectivities with a vertical resolution of 240 m and a horizontal resolution of 3 km. Due to CPR signal contamination at low altitudes and a lack of sensor sensitivity at high altitudes, the predictions are prone to lack shallow convection and ice clouds (Sassen and Wang, 2008; Haynes et al., 2009). To account for the attenuation, we use only 100 height bins of the CloudSat data predicting radar reflectivities between 2.4 and 24 km height on a scale between -25 and 20 dBZ (Bacmeister and Stephens, 2011). The temporal resolution of 15 min resembles the native temporal resolution of SEVIRI. While the original approach used data from 11 SEVIRI channels, we leave out channels with central wavelengths in the visible spectra to enable predictions at night time (Jones et al., 2023). Changes to the configuration for the ML model, input data and reported model error (RMSE) as described in the original paper can be found in Table 2. We detected no reduction in the model performance due to these modifications. Instead, the average error of the model decreases from 3.05 dBZ to 2.99 dBZ. The reported error is comparable to a precision of 5 dBZ achieved by other

Table 1. Overview of MSG SEVIRI channels (Schmetz et al., 2002).

Channel	Wavelength (μm)	Description	Spatial resolution at nadir	Retrieval at nighttime
VIS0.6	0.56-0.71	Visible channel	3 km	No
VIS0.8	0.74-0.88	Visible channel	3 km	No
NIR1.6	1.5-1.78	Near infrared window	3 km	No
IR3.9	3.48-4.36	Near infrared window	3 km	Yes
WV6.2	5.35-7.15	Upper-troposphere water vapour	3 km	Yes
WV7.3	6.85-7.85	Lower-troposphere water vapour	3 km	Yes
IR8.7	8.30-9.10	Mid infrared window	3 km	Yes
IR9.7	9.38-9.94	Ozone sensitivity	3 km	Yes
IR10.8	9.80-11.80	Clean longwave window	3 km	Yes
IR12.0	11.00-13.00	Dirty longwave window	3 km	Yes
IR 13.4	12.40-14.40	CO2 sensitivity	3 km	Yes
HRV	0.5-0.9	High-resolution visible	1 km	No

Table 2. Modifications to the Res-UNet originally proposed in Brüning et al. (2024)

Parameter	Original configuration	Modification
Number of input channels	11	8
Loss function	L2	L1
Nighttime predictions	No	Yes
Average RMSE	3.05	2.99

CloudSat products (Tomkins et al., 2024). We leverage the predicted data to detect and track convective clouds. Compared to methods based only on ground-based or active radar, the ML-based model can provide enhanced coverage of the contiguous 3D cloud field, especially over remote oceanic regions (Prein et al., 2024). We merge the 3D radar reflectivities along their temporal dimension to create a 4D time series used for further analysis.

3 Method

3.1 Tracking convective clouds in 4D

In this study, we analyse the spatio-temporal evolution of convective clouds by employing the *tobac* package (Heikenfeld et al., 2019). It is a modular Python-based package for tracking atmospheric objects in a 4D time series (Prein et al., 2024).

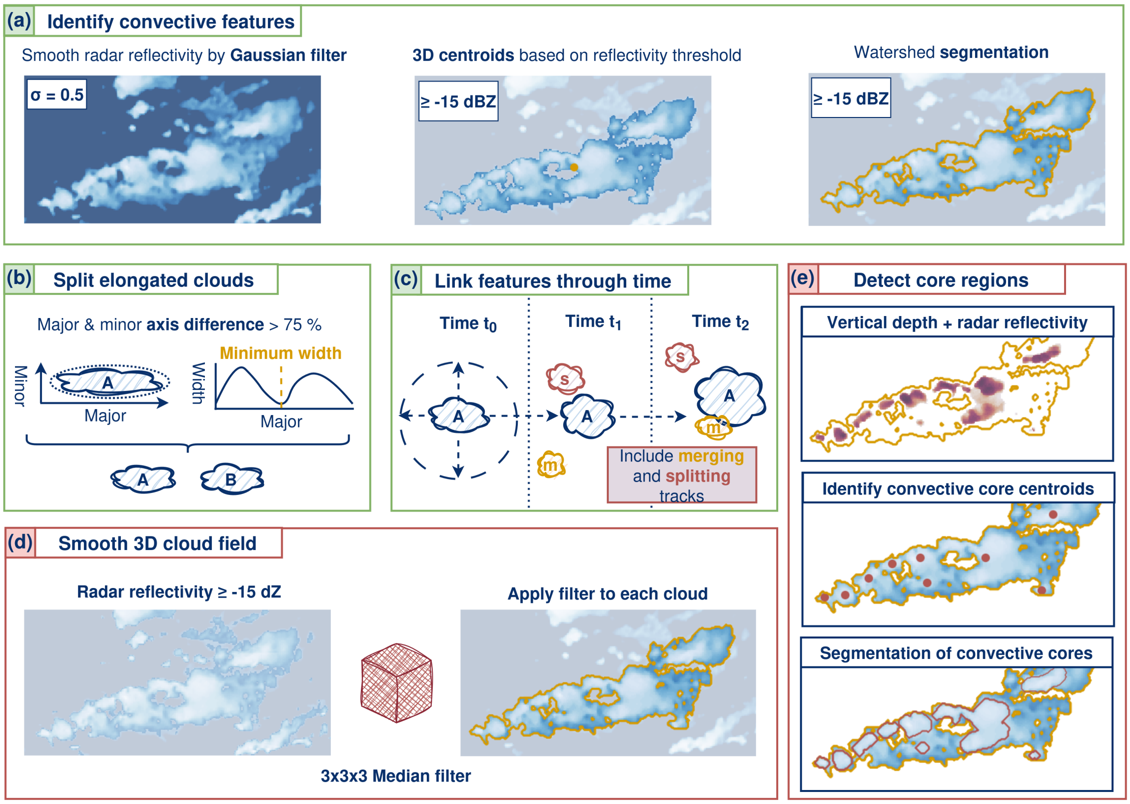

Figure 1. Workflow for tracking convective clouds **(a)**–**(c)** and their convective cores **(d)**–**(e)** using 4D radar reflectivities. The routine consists of **(a)** the identification and segmentation of convective cloud features using a threshold of–15 dBZ, **(b)** splitting elongated features along their major axis, and **(c)** linking the labelled cloud features through time. For detecting DCCs, we apply a fixed threshold of -15 dBZ. In **(d)**, we apply a Median filter with a kernel size of 3x3x3 pixels to each 3D cloud field. Following, the approach includes **(e)** calculating the number of contiguous pixels ≥ 0 dBZ for each vertical column and adding the cloud top radar reflectivity, to identify centroids of DCCs and to apply a watershed segmentation algorithm to derive the associated area for each core.

In this study, we use the recently released version 1.5 of the software package (Sokolowsky et al., 2024). It preserves the contiguity of the data in the horizontal and vertical dimensions, allowing an enhanced analysis of meteorological characteristics in 3D. We merge the predicted radar reflectivity along the temporal dimension and feed the 4D time series into the tracking algorithm to create continuous trajectories. The workflow consists of three steps: detecting cloud features by their centroid's position, segmenting the associated cloud field for each centroid, and linking segmented objects through time (Figure 1, a-c). We separate elongated cloud clusters if they are only connected by a few pixels in the horizontal and vertical dimensions to avoid incorrect label assignments (Oreopoulos et al., 2017). This workflow is depicted in Fig. 1 and will be explained in the following paragraphs.

3.1.1 Identifying cloud features

This study aims to reconstruct the cloud life-cycle from CI to the dissipation phase (Section 1). Although the radar reflectivity does not directly measure vertical velocity, it can be used as a proxy for convective intensity (Luo et al., 2008). For the cloud detection, we use a fixed threshold of -15 dBZ to differentiate signals from potential clouds and background noise within the radar reflectivities (Marchand et al., 2008). The threshold is weakly restrictive and might lead to the integration of short-lived features in the results (Sokolowsky et al., 2024). Nevertheless, we keep this threshold to detect and track the spatio-temporal evolution of convective clouds from CI to dissipation (Esmaili et al., 2016). At first, a Gaussian filter with a sigma filter size of 0.5 smoothes the input data (Kukulies et al., 2021). Afterwards, contiguous regions are labelled, applying the same threshold of -15 dBZ (Figure 1, a). The centroid of each feature is determined by the weighted mean of its position along three spatial dimensions (Heikenfeld et al., 2019). All centroids are assigned a unique identifier that is kept during the following steps. Following, we use a watershed segmentation to delineate the 3D cloud field associated to each centroid. The approach originates from geology and is used in image segmentation tasks. Here, the input data are treated as a topographic map divided into individual catchments along adjacent ridges (Meyer, 1994). We feed the 3D radar reflectivity image with the detected centroids into the watershed algorithm to delineate the pixels associated with each centroid (Jones et al., 2023). The value of each pixel is decreased towards its local minimum using a threshold of -15 dBZ. The result is a labelled cloud mask for each time step (Fiolleau and Roca, 2013). In a 3D cloud field, the number of pixels per centroid represents the cloud volume rather than the cloud area (Sokolowsky et al., 2024). In response, we calculate the aggregated 2D cloud anvil area using the column-wise maximum for further analysis (Table 3).

3.1.2 Split shallow connected clouds

After identifying the cloud centroids and associated cloud area, we analyse the morphology of each object. The goal is to separate elongated objects connected only at the location of the local minimum width of the cloud anvil (Figure 1, b). To detect these minima, we derive the best-fitting ellipse for each cloud (Ganetis et al., 2018). Then, we calculate the ratio between the major and minor cloud axes. If the difference between the axes is higher than 75 %, we consider the cloud elongated (Cui et al., 2021). The coordinates of the major axis give us the direction of elongation. Then, we determine the location of the split by analyzing the aggregated 2D cloud area and the change points of the area distribution. We perform no split if the distribution is unimodal with a single maximum. Otherwise, we split the cloud if the local minimum diverges by more than 75 % from the mean size of the cloud shield (Figure 1, b). We update the segmentation results by assigning an unique label to the separated objects.

3.1.3 Spatio-temporal linking

We link the 3D objects through time based on their movement speed (Heikenfeld et al., 2019). In contrast to a 2D linking routine, the 3D perspective enables an in-depth analysis of both the horizontal and vertical evolution, which is crucial for assessing the growth of DCCs (Fiolleau and Roca, 2013). For each 15-minute time step, we predict the movement of the objects

https://doi.org/10.5194/egusphere-2025-374
Preprint. Discussion started: 5 February 2025

based on their velocity in the previous time steps (Figure 1, c). We reduce the time needed for the search process by defining a maximum spatial radius between two consecutive time steps. Within this radius, potential links are identified and clouds are connected (Kukulies et al., 2021). Emerging clouds are assigned the average velocity of clouds in their neighbourhood (Sokolowsky et al., 2024). Due to limited computational resources, we only apply the linking for two consecutive time steps simultaneously. A temporal overlap of 15 minutes and a contiguous identifier determine whether to merge tracks. Afterwards, we check the cloud anvil area of linked objects to avoid false assignments. For that purpose, we apply a minimum area similarity of at least 50 % (Prein et al., 2024). Depending on the features' previous and subsequent movements, we estimate two objects to merge together or split off and include this information in the derived trajectories.

3.2 Detect convective core regions

After linking the trajectories, we apply a second detection algorithm to identify DCCs with a strong vertical ascent within the cloud's lower regions (Zipser and LeMone, 1980). A convective cloud typically contains one or more of these updraft regions with heavy rainfall that translates through the freezing level (Igel et al., 2014). The growth and decay of DCCs in these regions is particularly interesting for the intensity of convective clouds (Takahashi et al., 2017). In our study, we employ the ML-based radar reflectivity to identify the number and size of DCCs for each labelled cloud (Figure 1, d,e). We note that the radar reflectivity cannot replace a calculation of the vertical velocity. However, it provides information on the distribution of hydrometeors beneficial to estimate convective activity (Yuter et al., 2005; Luo et al., 2008). We mask reflectivities below -15 dBZ to detect convective core regions (Bacmeister and Stephens, 2011). Then, we apply a Median filter with a kernel size of 3x3x3 pixels to smooth the radar reflectivity (Tomkins et al., 2024). In our study, we identify a DCC in the 3D cloud field by a combined maximum of the column-wise aggregated radar reflectivity and the difference between the cloud top height (CTH) and cloud base height (CBH) for a vertically contiguous cloud layer (cloud vertical depth) (Takahashi et al., 2017).

As visualised in Fig. 1e, we start with counting the number of pixels ≥ 0 dBZ in each cloud column to estimate the cloud vertical depth (Tomkins et al., 2024). We expand the threshold from ≥ 0 dBZ to ≥ -5 dBZ if at least one pixel passes the first criterion (Igel et al., 2014). The cloud column is discarded if the CBH is ≥ 5 km or if the vertical profile shows no convective pixels for more than 50 % of the CTH (Masunaga and Luo, 2016). Otherwise, we add the mean radar reflectivity of the vertical profile to the derived vertical depth of the column (Oreopoulos et al., 2017). We search for local maxima of the combined cloud vertical depth and radar reflectivity to identify centroids of potential DCCs. Then, we mask the DCC area by a watershed segmentation. In case we find no maxima, the number of cores is set to zero (Feng et al., 2023). For all clouds with at least one DCC, we calculate the number of cores, core area, core vertical depth, and core lifetime (Table 3). For more than one DCC, we additionally derive the mean distance between DCCs (Bacmeister and Stephens, 2011).

3.3 Extract cloud and core properties

For each trajectory along space and time for an individual detected object, we extract the associated cloud and core properties as displayed in Table 3. While some of these properties can be derived from 2D data by analysing peaks in e.g., the IR spectra of geostationary satellites, approximating the vertical column is often error-prone, e.g., when cirrus at the cloud top layer are mistaken for deep convection. For instance, ground-based radar receive 3D data which can be used to assess the cloud vertical structure. However, they deliver only few information about clouds developing over remote oceanic regions. Most passive and active sensors lack the data coverage to enable a seamless analysis of the 3D convective cloud structure over different surface types. Our approach allows for a more holistic perspective on cloud development over land and sea. We may derive horizontal cloud properties, like the anvil area or cloud eccentricity, and vertically resolved properties, like the CTH, simultaneously (Table 3). Furthermore, analysing the structure of DCCs by our 3D data may deepen the insights on convective activity in convective core regions. We employ the radar reflectivity at a fixed altitude of 10 km as a measure of convective activity. The ratio between the major and minor cloud axes are used to calculate the eccentricity which describes the best fitting ellipse for the cloud. Values range between 0–1, with higher values indicating a more spherical shape (Cui et al., 2021). For convective clouds, the eccentricity may affect its hazard potential (Gallus et al., 2008). For example, linear convective systems are more prone to heavy wind and precipitation (Semie and Bony, 2020). Additionally, we calculate the ratio between the area of the convective core and cloud anvil as a measure of convective strength and compactness (Haberlie and Ashley, 2018).

Table 3. Features used to describe the morphology, physical properties, and life-cycle transition statistics of convective clouds and cores.

Feature type	Feature name	Definition
Cloud	Cloud area	Area of the cloud anvil (km^2)
	Cloud top height (CTH)	Maximum height of the cloud (km)
	Cloud base height (CBH)	Minimum height of the cloud (km)
	Area ratio	Ratio between cloud anvil area & DCC area
	Eccentricity	Roundness of the best fitting ellipse (cloud)
	Reflectivity	Average radar reflectivity of the cloud at 10 km height (dBZ)
	Location	Longitude and latitude of the cloud centroid (°)
	Travel distance	Euclidean distance for coordinates at initiation and dissipation (°)
	Cloud lifetime	Lifetime of the cloud trajectory (h)
	Surface type	Value of the land-sea mask
Core	Number of cores	Number of identified convective core regions
	Core size	Average size of convective cores (km^2)
	Core vertical depth	Depth of the DCC in the vertical column (km)
	Mean distance	Average distance between DCCs in a cloud cluster (km)
	Core lifetime	Average lifetime of the DCCs (h)
	Core eccentricity	Roundness of the best fitting ellipse (core)
Life-cycle	Cooling	Reflectivity change at 10 km height (dBZ)
	Area growth	Relative cloud area expansion (%)
	Vertical growth	Vertical growth of the cloud (km)

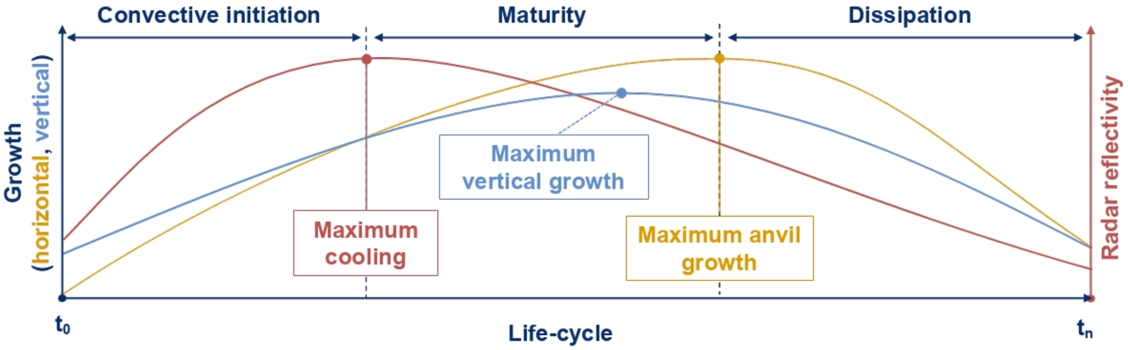

Figure 2. Schematic visualisation of the three stages of the convective life-cycle. We show the changes of the cloud anvil areal and the radar reflectivity at 10 km that induce a transition between convective initiation (CI), maturity (MAT), and dissipation. Additionally, we include the vertical growth of convective clouds derived from the 3D radar reflectivites.

We divide the life-cycle of convective clouds in three phases and assess spatio-temporal changes of the cloud properties as shown in Fig. 2. The first time step of the trajectory defines the beginning of the convective initiation (CI) (Futyan and Genio, 2007). For each point in time, we calculate the difference between the radar reflectivity at 10 km height at CI and the current time step to approximate the cooling of the convective cloud. Furthermore, the 3D data allows us to simultaneously derive the vertical growth of the cloud. It describes the difference between the CBH and CTH at CI for each time step, compared to CI. The highest difference of the radar reflectivity displays the maximum cooling and induces a transition between the CI and the maturity phase (MAT) (Takahashi et al., 2023). During the MAT, the horizontal growth of the cloud anvil increases. The end of the MAT is marked when the cloud anvil reaches its maximum relative size compared to the anvil size at CI. We further track the cloud until dissipation and we detect no more cloud centroid $\geq$ -15 dBZ (Crook et al., 2019). For each trajectory, we derive the point in time where transitions occur between life-cycle phases (maximum cooling, maximum anvil growth, maximum vertical growth, dissipation). Additionally, we determine the point in time with the highest number of DCCs and maximum DCC size to compare statistics for isolated and clustered clouds.

3.4 Filter convective cloud trajectories

We filter the trajectories based on morphological and microphysical cloud properties (Section 3.3) to exclude non-convective tracks from the analysis (Figure 3). We select all tracks that show at least one DCC and a reflectivity peak of $\geq$ 0 dBZ at 10 km height for at least 15 min along the trajectory (Igel et al., 2014). Additionally, we apply a minimum CTH of 10 km to account for the typical convective properties within the tropics (Li et al., 2021). A maximum CBH of $\leq$ 5 km is used to discard clouds without an evolved cloud base (Bacmeister and Stephens, 2011; Takahashi et al., 2023).

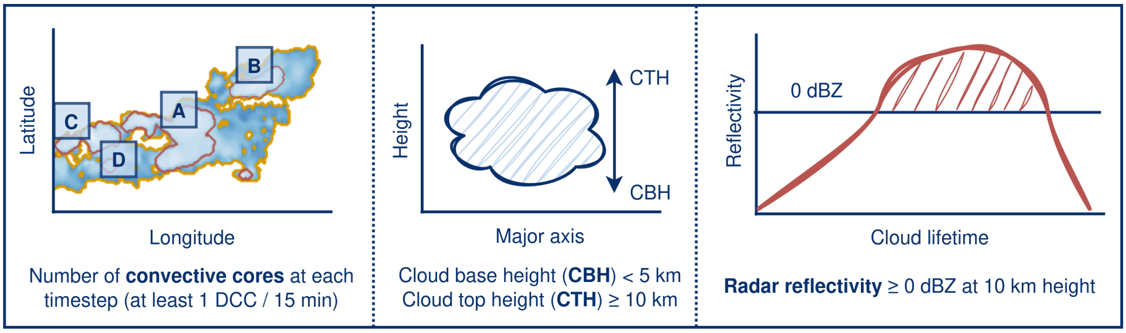

Figure 3. Criteria for filtering convective clouds from the derived trajectories. These consist of counting the number of convective cores (A-D) for each cloud whereas we require minimum of ≥ 1 DCC to pass as a convective cloud. We check the cloud base height (CBH) and cloud top height (CTH) of the cloud, and the radar reflectivity at 10 km height along the cloud trajectory.

4 Results

4.1 Evaluation of convective cloud trajectories

From March to August 2019, we detect 375 000 convective clouds. Figure 4 shows an example of the tracked DCCs and their associated anvils. We observe a high number of convective clouds over the Gulf of Guinea, the equatorial rainforest, and the Atlantic Ocean. As seen over Marocco and Mauretania, a high radar reflectivity at the cloud top does not necessarily indicate the presence of a deep convective system (Kukulies et al., 2021). In Fig. 4b–4e, we zoom in to observe the evolution of the cloud systems in 3-hourly intervals. Our findings show that DCCs often persist only for a short time. Furthermore, we may find several DCCs within MCSs at the same time which indicates a higher convective activity in the cloud cluster compared to the presence of a single DCC (Takahashi et al., 2017).

We extract the 3D properties not only for the cloud anvil but also for each DCC. Our 3D perspective allows to track the cloud's horizontal and vertical development simultaneously (Takahashi et al., 2023). To derive statistics for the DCCs, we separate the core region from the anvil cloud, as visualised in Fig. 5.

We group the detected clouds based on the number of associated DCCs to differentiate isolated clouds with a single DCC and clustered systems with multiple DCCs (Li et al., 2021). Clouds with 6–9 cores and those with ten or more cores are grouped for the statistical analysis (Jones et al., 2024). Most of our trajectories (80 %) contain clouds with a single core (Figure 6, a). The proportion considerably declines with an increasing number of DCCs. Clouds with ten or more DCCs account for about 10 % of all trajectories. Figure 6b shows the lifetime grouped in 3-hourly intervals. Deep convection generally appears on a wide range of scales, whereas most clouds are short-lived, with a lifetime of up to 3 h. For higher lifetimes, the proportion of trajectories steadily decreases. The distribution of the surface type is analysed in Fig. 6c. About 70 % of our tracks are located over sea and 30 % over land. Compared to the actual land surface distribution, we observe a shift of about 5–10 % towards the sea as convective systems in tropical Africa propagate towards the Atlantic Ocean. The difference between single-

https://doi.org/10.5194/egusphere-2025-374
Preprint. Discussion started: 5 February 2025

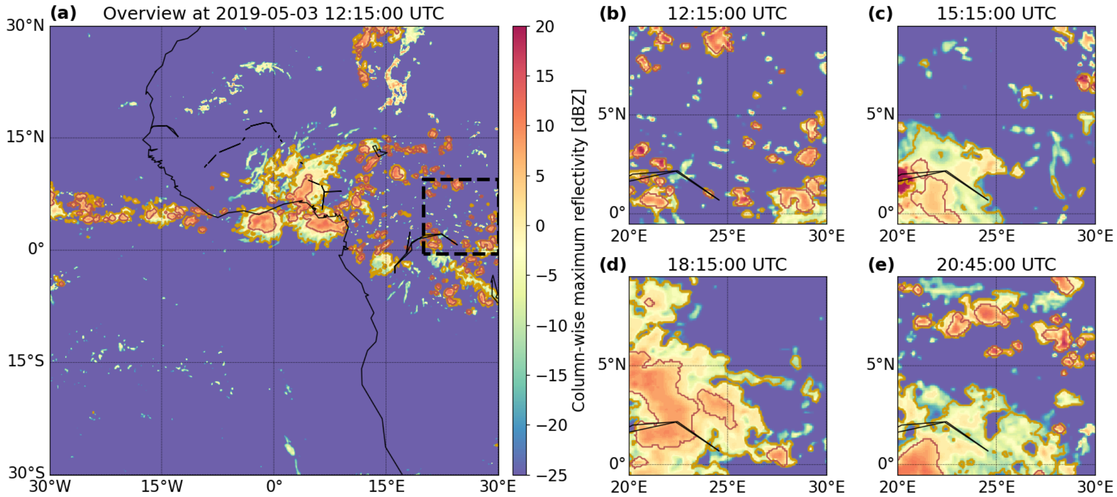

Figure 4. An example of convective clouds (orange outline) and their cores (red outline) detected by the tracking approach for the 03.05.2019 12:15:00 UTC. The cloud mask is plotted over the 3D radar reflectivity aggregated by the column-wise maximum. All times are given in UTC. In **(a)**, we see an overview of the AOI, **(b)** to **(e)** show a zoomed perspective in 3 h intervals (black square).

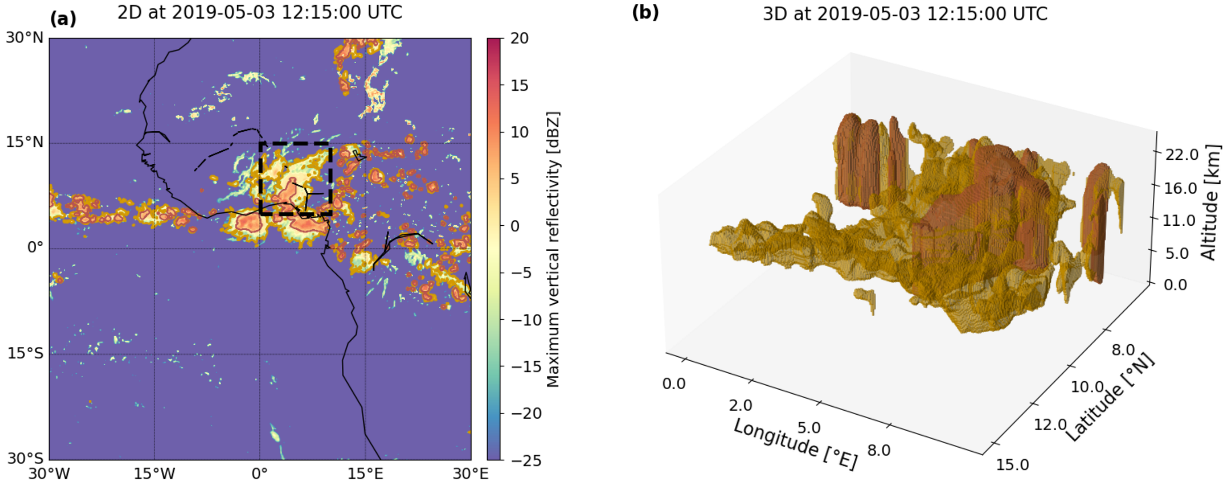

Figure 5. An example of the convective clouds (orange outline) and their cores (red outline) detected by the tracking approach for the 03.05.2019 12:15:00 UTC. The cloud mask is plotted over the 3D radar reflectivity aggregated by its cloud top maximum. In **(a)**, we see an overview of the AOI, **(b)** shows the zoomed perspective (black square) in 3D for the cloud volume (orange) and core volume (red).

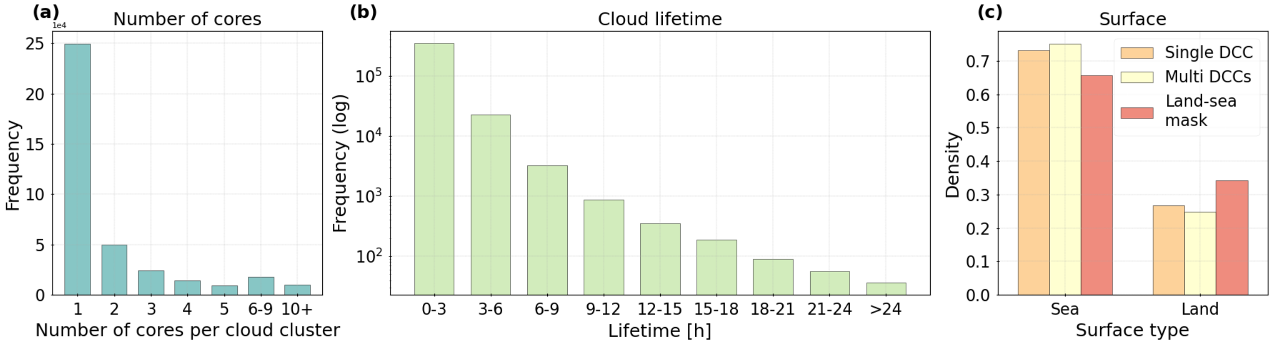

Figure 6. Cloud statistics for **(a)** the number of associated cores, **(b)** the average cloud lifetime on a logarithmic scale, and **(c)** the distribution of the surface type derived from a land-sea mask compared to the location at CI for single- (1 DCC) and multi-core (> 1 DCC) clouds.

and multi-core clouds accounts for up to 5 % over each surface type. We observe slightly more isolated cells over continental Africa and more clustered systems over the Atlantic Ocean. This finding emphasises we may find more favourable conditions for the development of intense convective clusters over the ocean (Cui et al., 2021).

We analyse the distribution of the 3D cloud physical properties for different numbers of DCCs (Table 3). For isolated clouds with a single DCC, we observe a substantially shorter lifetime and travel distance than for clusters with several DCCs, particularly for clusters with more than 10 DCCs (Figure 7,a–b). In contrast, the cloud eccentricity is less dependent on the number of DCCs (Figure 7,c). For all groups, we see an eccentricity between 0.6–0.7, with only a singular peak at 0.8 for single-core clouds. The cloud anvil area varies considerably stronger between each DCC group than the roundness of the clouds. Most single-core clouds have an anvil area $\leq 1\,000$ km^2. The area increases with the number of DCCs, especially for clouds with more than 10 DCCs (Figure 7,d). For instance, the anvil size and CTH are 10–20 % higher over the land than sea. The radar reflectivity at 10 km height increases with the number of cores, in particular for highly clustered systems (Figure 7,e). It is on average 0.5 dBZ higher over the ocean than over land. Overall, differences in the intensity of convection are higher between isolated and clustered clouds than for different surface types.

Moreover, our approach allows us to simultaneously investigate the core properties for isolated and clustered clouds. Figure 8a shows the average core lifetime between initiation and dissipation. Long-lasting clouds are connected a longer core lifetime. For single-core clouds, the core persists on average for 0.3–0.4 h. The core lifetime and eccentricity increase according to the cloud lifetime in Fig. 8 to 1.2 h for clustered clouds. More and long-lasting cores come along a higher vertical depth (Figure 7,d). Over the sea, cores are more extensive for less clustered clouds. In contrast, the core size over land increases stronger with many cores. This growth is induced by drier surface conditions and a higher lifting condensation level over land, promoting a stronger convective updraft (Takahashi et al., 2017). As the core area grows, the distance between the cores increases, especially for convective clouds over land (Figure 8,e). The ratio between the core and anvil area depends on the number of DCCs and the surface type. Overall, it is higher over the ocean (Figure 8,f). For clouds with ≥ 2 DCCs, the ratio lies at 10 % or less, while we observe a ratio of 25 % for single-core clouds. An enhanced convective activity comes along with a lower area ratio,

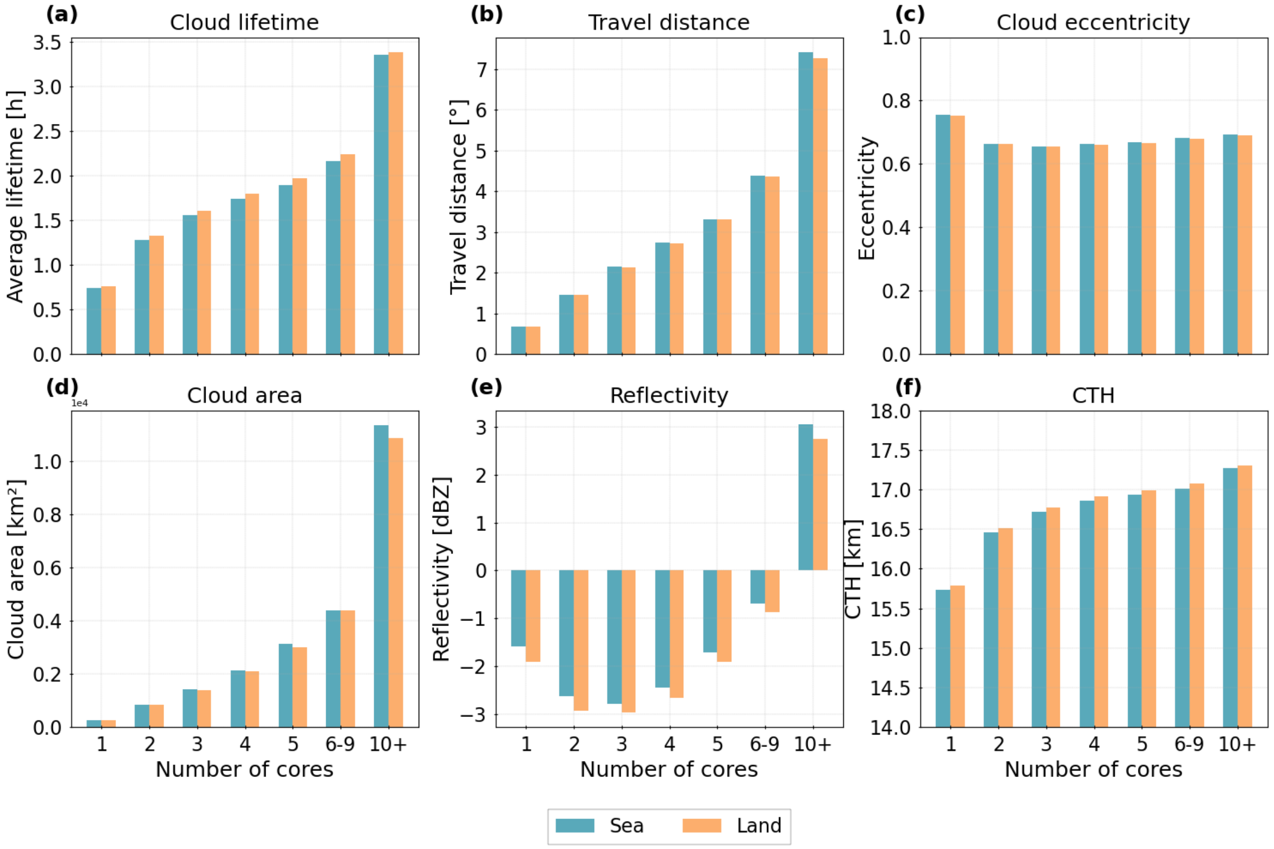

Figure 7. Cloud statistics grouped by the number of associated cores for **(a)** the cloud lifetime, **(b)** the travel distance from CI to dissipation, **(c)** the cloud eccentricity, **(d)** the cloud anvil area, **(e)** the radar reflectivity at 10 km height, and **(f)** the CTH.

280 indicating a larger anvil outflow compared to the DCC size (Horner and Gryspeerdt, 2023). The core properties indicate on average a stronger convective activity over continental Africa, in particular when comparing highly clustered cloud systems.

4.2 Temporal characteristics of tropical convection

4.2.1 Diurnal cycle over land and sea

We compare the diurnal cycle for single-core and multi-core clouds over sea and land. Figure 9 shows the cloud lifetime, 285 the cloud anvil area, and the radar reflectivity at 10 km height. For isolated clouds over land, we see a peak for the radar reflectivity and the cloud anvil area beginning in the early afternoon (Figure 9,f,j). Continental clouds have a larger anvil area and lower reflectivity compared to clouds over the ocean. This deviation may originate an enhanced local thermal instability (Cui et al., 2021). During the afternoon, environmental conditions favour the initiation of convection over land. In contrast, a more steady sea surface temperature is responsible for convective clouds developing over the ocean. Although the distribution

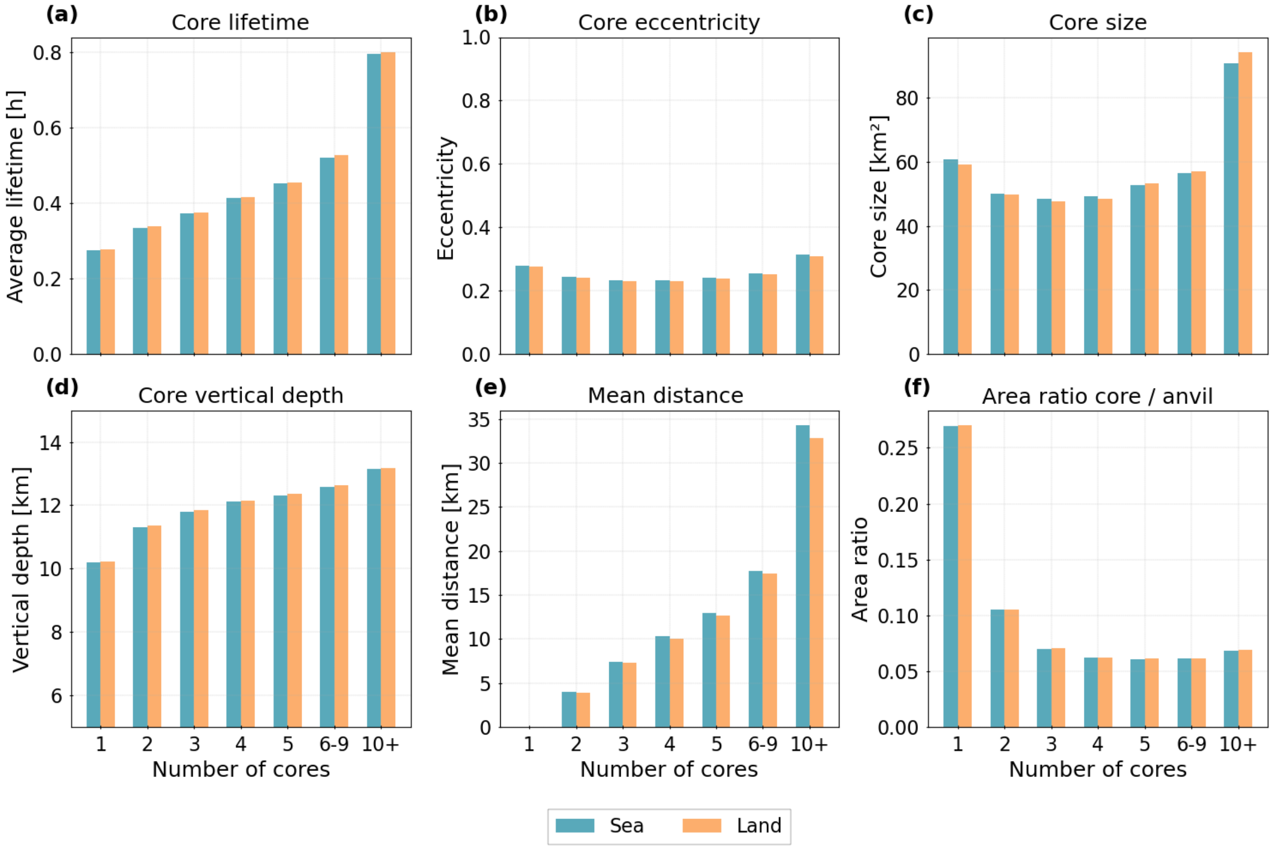

Figure 8. Core statistics grouped by the number of associated cores for **(a)** the core lifetime, **(b)** the core eccentricity, **(c)** the core area, **(d)** the vertical depth of the core, **(e)** the mean distance between individual cores, and **(f)** the area ratio between the cloud anvil and the core.

shows a bimodal diurnal cycle with two pronounced peaks in the night and late afternoon, the formation of DCCs over the sea can occur at any time of day due to their linkage to external forcing like cold pools (Chen and Houze, 1997). Between midnight and early morning, a pronounced cooling over land reverses the land-ocean circulation. The radiative cooling at the cloud top destabilizes the boundary layer and promotes the development of oceanic convection. After sunrise, incoming solar radiation at the cloud top increases the stability and depresses the development of convection. With a weakened land breeze in the morning hours, the nocturnal convective clusters over the ocean dissipate (Houze Jr., 2004). We observe this diurnal pattern for isolated clouds, in particular. Clustered clouds have a substantially larger anvil area and higher reflectivity at 10 km height (Figure 9,g,h,k,l). Although the diurnal cycle is similar for clouds with multiple DCCs, the diurnal variability of the reflectivity is smaller than for isolated clouds. Isolated clouds have a higher eccentricity than clustered clouds (Figure 9,a–d). Especially during peak times over sea and land, we observe an enhanced axes ratio of up to 0.9. For both surface types, an increasing number of DCCs induces a temporal shift of the afternoon peak within the radar reflectivities and the anvil area (Figure 9,k–l).

https://doi.org/10.5194/egusphere-2025-374
Preprint. Discussion started: 5 February 2025

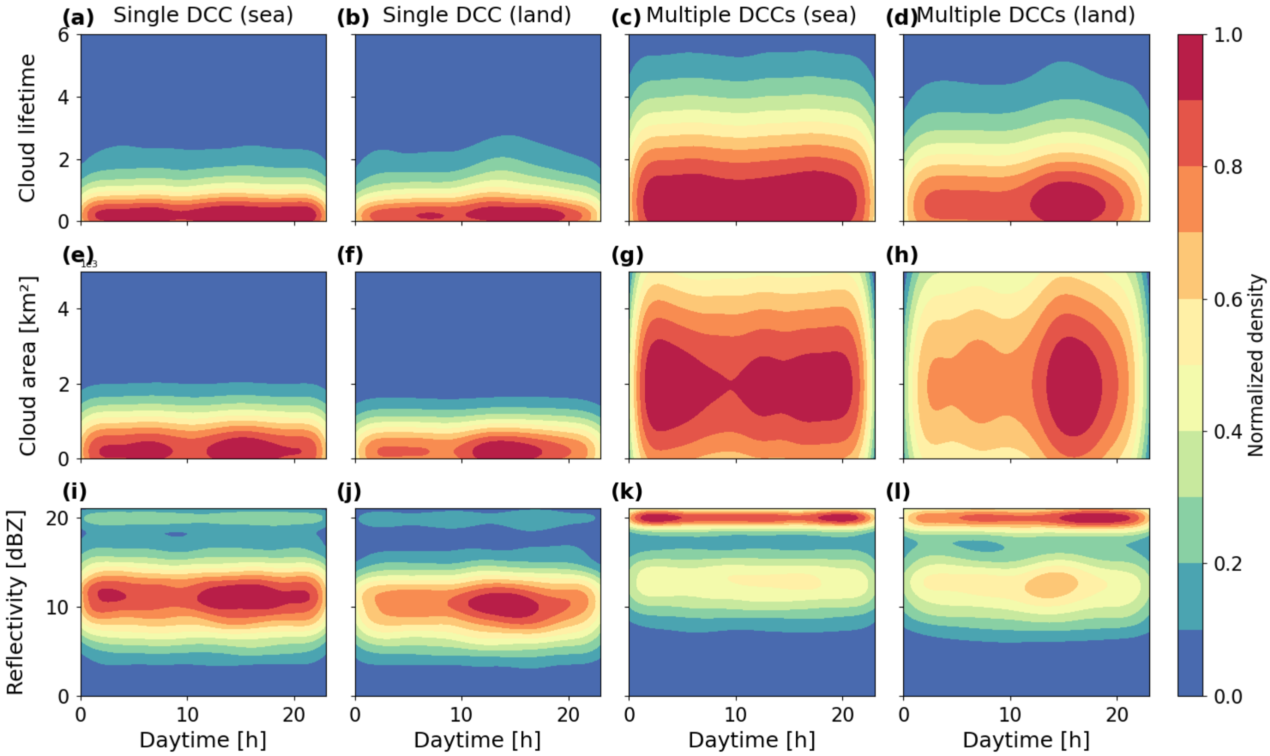

Figure 9. Diurnal cycle for cloud properties grouped by the number of associated cores and surface type. We display the hourly changes regarding **(a)**–**(d)** the cloud lifetime, **(e)**–**(h)** the cloud anvil area, and **(i)**–**(l)** the radar reflectivity at 10 km height for single- (1 DCC) and multi-core (>1 DCC) clouds over sea and land. The values show the density distribution of each parameter normalized between 0 and 1.

We use our data to estimate not only horizontally resolved cloud properties, but to also extract the 3D properties of the DCCs. The diurnal pattern resembles those of the cloud properties. The core size, core lifetime, and core eccentricity show a bimodal distribution over the sea and a singular afternoon peak over land (Figure 10,a–l). An increased number of DCCs comes with larger cores and an enhanced lifetime, particularly for clouds over land. For clustered clouds over land, we see a second maximum at night, which typically appears over sea surfaces. However, the afternoon peak is consistently more powerful (Figure 10,c–d). The core eccentricity of isolated clouds shows a higher variability and a lower mean than for clustered clouds (Figure 10,i–l). The core and anvil area ratio shows a comparable primary peak between 0–0.1 for all types. Single-core clouds have a secondary peak at 0.5, pointing out the simultaneous existence of clouds with different shapes and life-cycle phases (Figure 10,m–p). Cores are more extensive and persistent over land, reflecting the contrast between convective intensity over land and sea (Vondou, 2012).

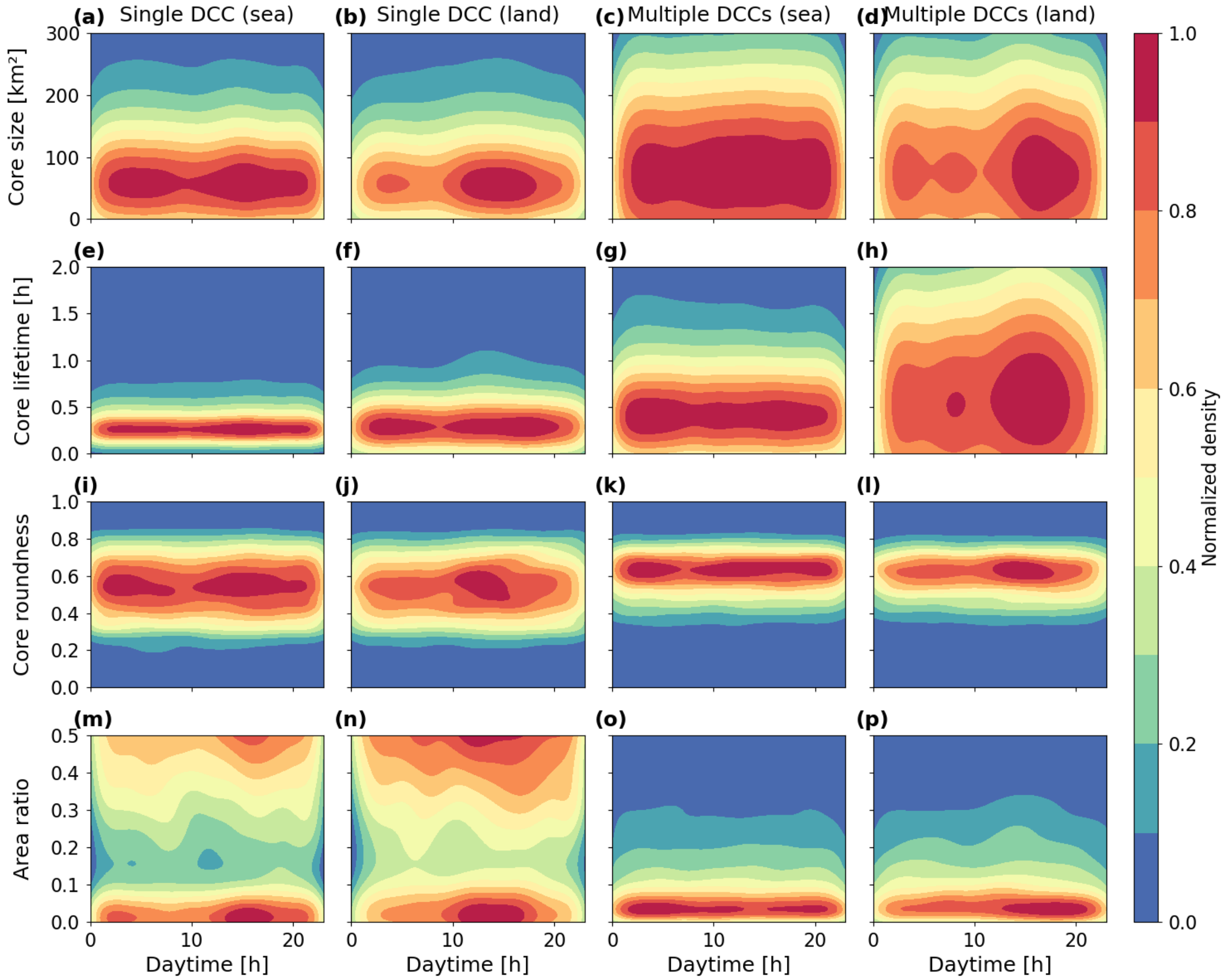

Figure 10. Diurnal cycle for core properties grouped by the number of associated cores and surface type. We display the hourly changes regarding **(a)**–**(d)** the core size, **(e)**–**(h)** the core lifetime, **(i)**–**(l)** the core eccentricity, and **(m)**-**(p)** the area ratio between the cloud core and anvil area for single- (1 DCC) and multi-core (>1 DCC) clouds over sea and land. The values show the density distribution of each parameter normalized between 0 and 1.

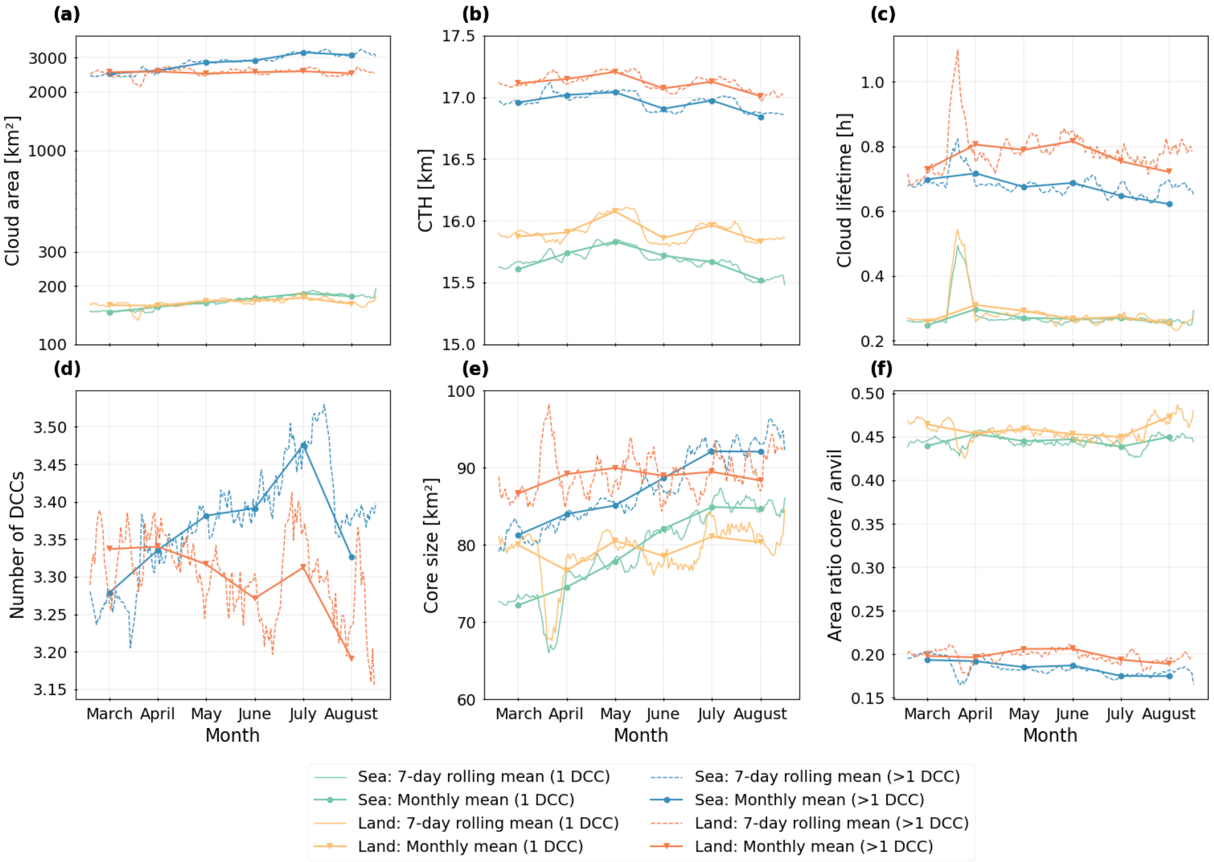

Figure 11. Seasonal variability of cloud and core statistics between March and August grouped by the surface type for **(a)** the cloud anvil area, **(b)** the CTH, **(c)** the cloud lifetime, **(d)** the number of DCCs, **(e)** the core size, and **(f)** the area ratio between the cloud anvil and the core. We show the monthly mean (solid lines) and 7-day rolling mean (dashed lines) for the time series for single- and multi-core clouds over land and sea.

4.2.2 Seasonal variability of convective clustering

Within the tropics, the seasonal cycle of atmospheric processes substantially affects convective cloud and core development (Andrews et al., 2024). In Fig. 11, we calculate the monthly average and a rolling mean for a 7-day window for the cloud area, the CTH, the number of DCCs per cluster, the core size, core lifetime, and the area ratio between cores and cloud anvils. Overall, convective activity increases in summer by about 5–10 %. An enhanced core size and a decreased area ratio between cores and anvils accompany an increased average cloud anvil area. At the same time, the number of DCCs increases over the ocean and decreases over the land. The CTH shows a bimodal distribution with peaks in May and July. We observe a higher CTH, cloud lifetime, and area ratio over land throughout the depicted time series. The differences between land and sea are less distinct regarding the number of DCCs, their size, and the cloud area.

https://doi.org/10.5194/egusphere-2025-374
Preprint. Discussion started: 5 February 2025

In Fig. 12, we compare the differences for the cloud and core properties over sea and land. For that purpose, we average the data on a monthly basis. The results are displayed in 3-hourly intervals. For most parameters, we observe that direction changes occur on a seasonal basis. The diurnal variability show less distinct patterns than the seasonal changes. Continental clouds have more extensive anvils and a higher CTH and cloud lifetime (Figure 12,a–c). However, oceanic clouds become larger than clouds over land in summer (JJA) (Figure 12,a). Overall, the DCC properties show a higher seasonal dependency. In spring, continental clouds come with more DCCs, larger cores, and a lower area ratio than cloud over the ocean (Figure 12,d–f). In summer, the pattern reverses. This finding suggests that clouds appear more clustered over land in spring (MAM) and the ocean in summer (JJA).

4.3 The influence of DCCs on the cloud life-cycle

We use the criteria defined in Sect. 3.3 to assess the transition between the three life-cycle phases dividing each cloud into a growing, a mature, and a dissipation phase. We calculate for each cloud the maximum cloud cooling, maximum area expansion of the anvil, and the final dissipation of the cloud (Futyan and Genio, 2007). Moreover, the 3D data allow us to derive the maximum vertical growth (Figure 2). We detect an average cooling (in terms of a change in reflectivity as depicted in Table 3) of 10–14 dBZ at 10 km height (Figure 13,a). This cooling is enhanced for isolated clouds, particularly over the ocean, and over land for clustered clouds with ≥ 4 DCCs. We derive the area growth of the cloud anvil after the time of the maximum cooling. The average growth for all clouds accounts for 20–60 % compared to the anvil area at CI. We find the highest values for clouds with more than 5 DCCs. The vertical growth shows a reversed pattern as clouds with fewer DCCs tend to have a stronger vertical growth between CI and the time of maximum cooling (Figure 13,c). For all clouds, the growth of the anvil and the vertical growth are higher over land due to a more pronounced thermal instability and surface heating during the day(Takahashi et al., 2017).

In Fig. 14, we compare the convective cloud life-cycle grouped by the number of DCCs. For that purpose, we derive the time of transition between the three life-cycle phases and the dissipation time for each group. Additionally, we include the life-cycle of the cloud clustering by assessing the time when we find the most and largest DCCs. Overall, we observe a broadening distribution and a shift towards a later occurrence for each phase with increasing numbers of DCCs. Multiple peaks characterise the distribution for single-core clouds. In contrast, clustered clouds show a smoother uni- to bimodal distribution. In all cases, the average time of maximum cooling and maximum vertical growth occurs before the maximum area growth. This finding indicates that the anvils continue growing beyond the time of maximum convective activity. All clouds reach their maximum core size before the time of the maximum anvil area growth. In contrast to the core size, the time of the maximum core number varies with the number of DCCs. For less clustered clouds, the time of the maximum core number and the maximum vertical growth are similar. With a higher degree of organisation, the maximum number of cores appears after the maximum area growth. The continuous interaction of convective cores within clustered clouds may prolong the life-cycle due to a regeneration of convective intensity (Takahashi et al., 2017). As the cloud lifetime increases with the number of associated cores, the cooling and area growth appear earlier during the relative cloud lifetime. Clustered clouds spend more of their life-

https://doi.org/10.5194/egusphere-2025-374
Preprint. Discussion started: 5 February 2025

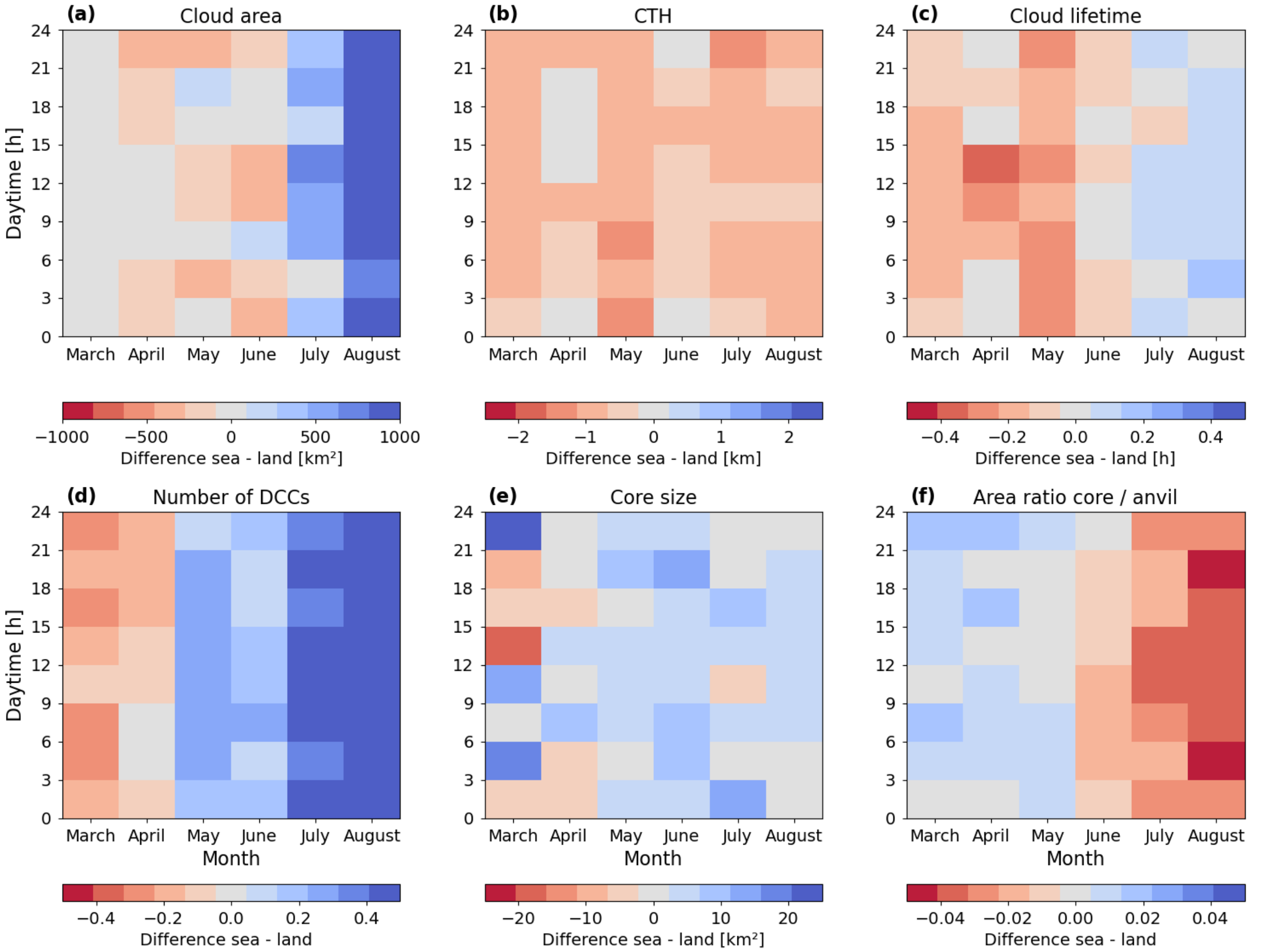

Figure 12. Differences between oceanic and continental cloud and core properties. Data is averaged on a monthly basis between March and August and grouped in 3-hourly intervals for **(a)** the cloud anvil area, **(b)** the CTH, **(c)** the cloud lifetime, **(d)** the number of DCCs, **(e)** the core size, and **(f)** the area ratio between the cloud anvil and the core.

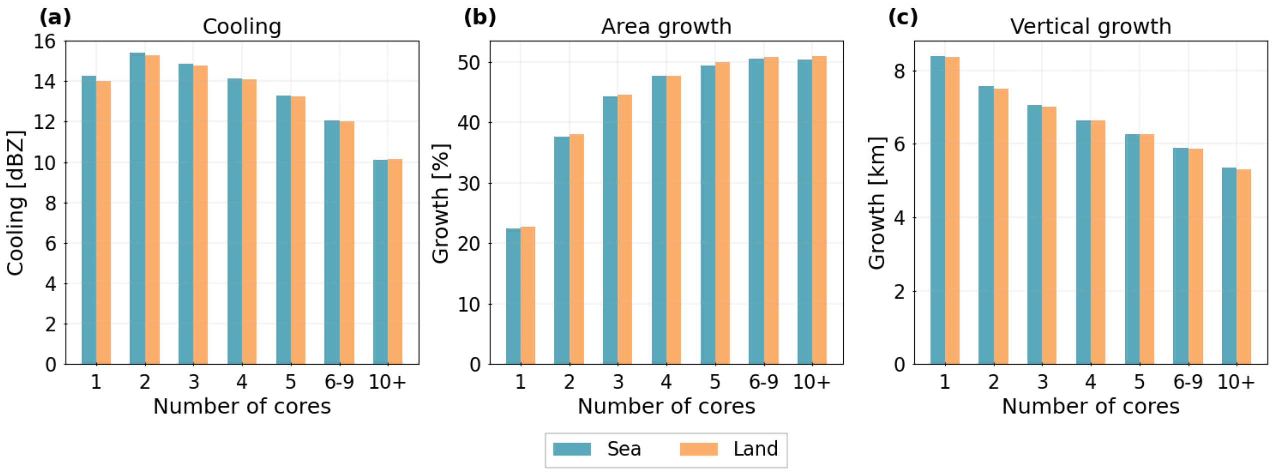

Figure 13. Life-cycle phase transition statistics grouped by the number of associated cores for **(a)** the maximum cooling at 10 km height, **(b)** the relative area expansion, and **(c)** the vertical growth of the cloud.

cycle in a dissipating phase with a warming, shrinking anvil than a single-core cloud. As ≥ 80 % of detected clouds contain a single DCC, these isolated clouds considerably affect the mean calculated for all clouds (Section 4.1).

In Fig. 15, we analyse the diurnal cycle for the maximum cooling, area growth, and vertical growth grouped by the surface type for isolated and clustered clouds. The distribution of these life-cycle statistics is similar to the diurnal convective cloud development over land and sea (Cui et al., 2021). We observe a morning peak followed by a decrease in the afternoon for the maximum cooling and vertical growth, particularly for single-core clouds. A subsequent anvil area growth follows cooling phase (Figure 14). Over the ocean, we observe a weak diurnal cycle with a primary peak in the late afternoon and a secondary peak at night. Overall, the vertical growth and absolute cooling are stronger for isolated clouds (Figure 15,a–c). Clouds with a single core show a reflectivity difference of up to 14 dBZ between CI and MAT and a vertical growth of 5.6–7 km. With an increasing number of DCCs, the total cooling and vertical growth of each DCC decreases as prior convective activity already induced a higher average radar reflectivity. In contrast, the anvil growth is on average 15 % higher for clustered systems. All continental clouds show a maximum anvil growth in the early afternoon. Over the ocean, the diurnal peaks are weaker with a slight shift towards the late afternoon and early evening (Figure 15,b,e).

The seasonal cycle shows an increased cooling of about 2 dBZ and vertical growth of about 1–1.5 km between spring and summer (Figure 16). For the area growth, we see an increase between 5–10 % for clustered clouds over land and sea and a decrease of 3–10 % for isolated cells over land. Throughout the time series, the cooling and vertical growth are higher for clouds with a single core. Clustered clouds have a weaker maximum cooling and vertical growth. However, they show a more extensive area growth. A higher cooling, horizontal, and vertical growth of clustered clouds is associated with higher convective activity and more intense DCCs. While convective activity increases over the ocean in summer, we still detect more intense

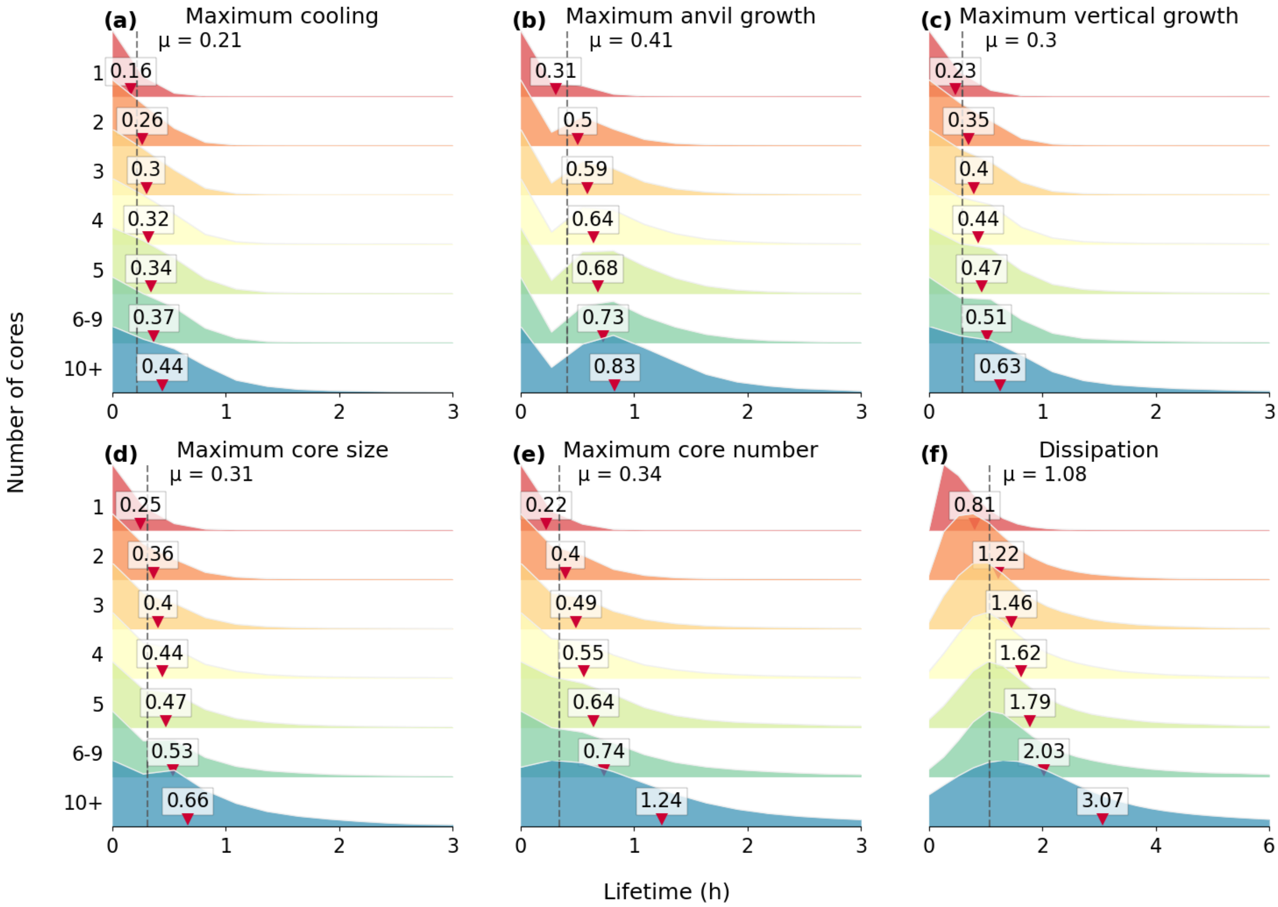

Figure 14. Ridgeplot showing the time dependency (x-axis) of the life-cycle phase transition statistics for **(a)** the maximum cooling at 10 km, **(b)** the maximum vertical growth, **(c)** the maximum anvil growth, **(d)** the maximum core size, **(e)** the maximum core number, and **(f)** the dissipation time grouped by the number of cores. The vertical lines show the mean time for all clouds, the red triangles the mean for each DCC group.

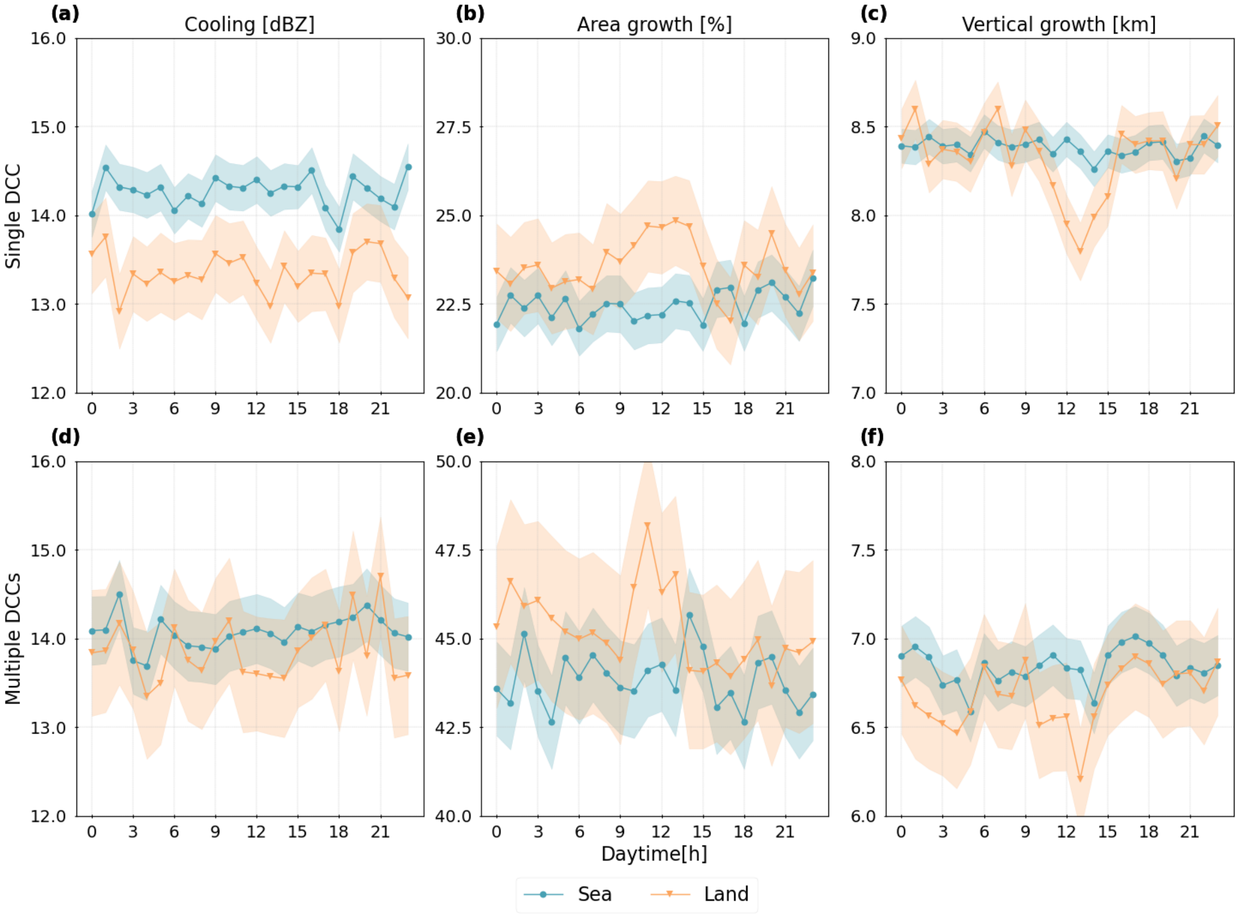

Figure 15. Diurnal cycle for the indicators showing the transition between cloud life-cycle phases. The data is grouped by the number of associated cores and the surface type. We display the hourly changes regarding **(a)** & **(d)** the maximum cooling, **(b)** & **(e)** the cloud anvil area growth, and **(c)** & **(f)** the cloud vertical growth for single- (1 DCC) and multi-core (>1 DCC) clouds over sea and land. Line plots show the mean value with a confidence interval of 95 %.

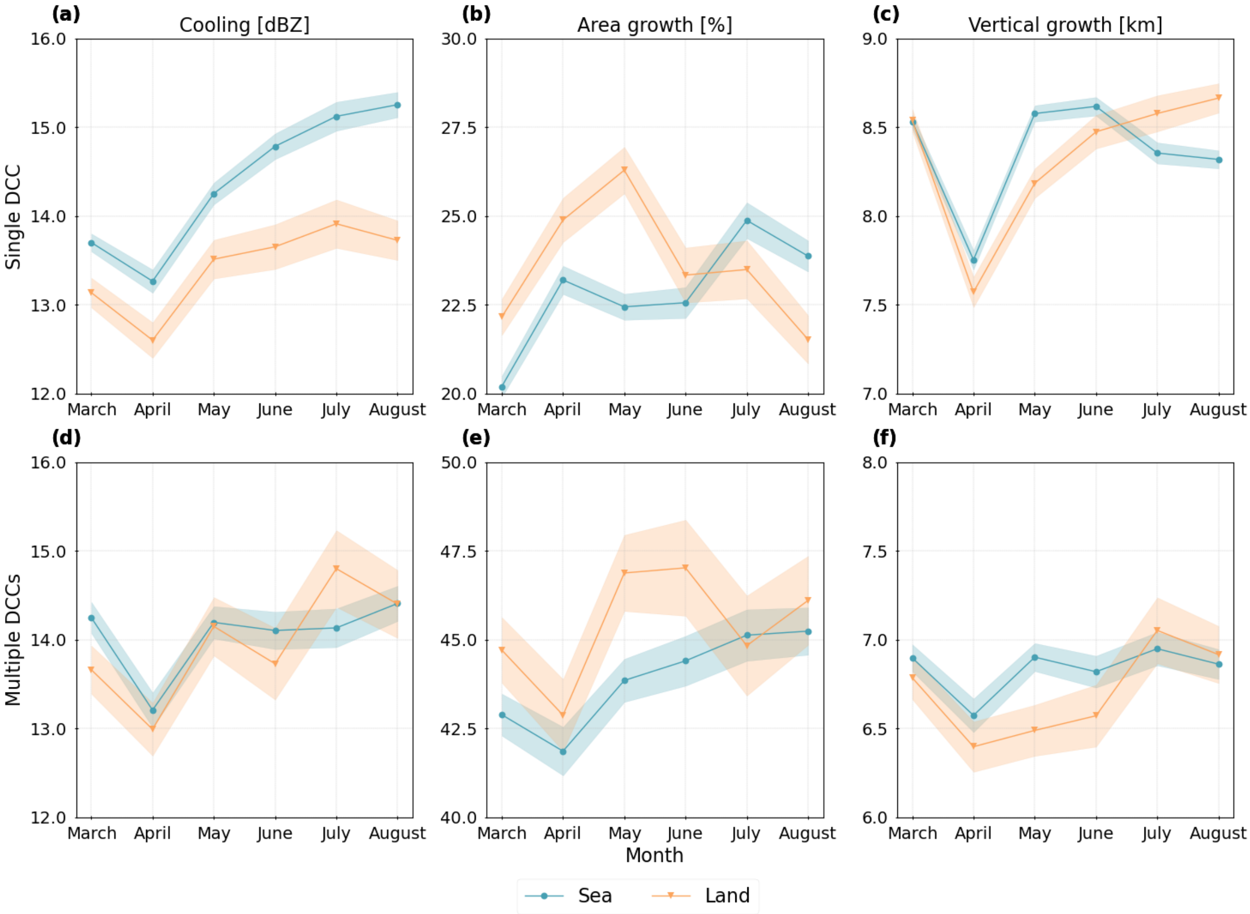

Figure 16. Seasonal cycle for the indicators showing the transition between cloud life-cycle phases. The data is grouped by the number of associated cores and the surface type. In **(a)** & **(d)**, we show the maximum cooling, in **(b)** & **(e)** the anvil area growth, and in **(c)** & **(f)** the vertical growth for clouds with a single (1 DCC) core or multiple (>1 DCC) cores. Line plots show the mean value with a confidence interval of 95 %.

changes in the cloud life-cycle over land (Figure 15, 16). The difference may be due to a higher variability of the moisture availability over land and an enhanced orographic forcing (Chen et al., 2021).

5 Discussion

375 Our analysis provides a detailed perspective on the temporal variability of deep convective cells and associated core regions derived from ML-based 3D radar reflectivities. In previous studies, retrievals of DCCs often originate 2D data, either from geostationary satellites (Jones et al., 2024; Vondou, 2012) or from active radar, such as the CloudSat CPR (Igel et al., 2014;

https://doi.org/10.5194/egusphere-2025-374
Preprint. Discussion started: 5 February 2025

Takahashi et al., 2017). These approaches are limited to comprise either a specific horizontal or vertical dimension. As a result, they cannot provide a seamless coverage of the cloud development. With geostationary satellites, we can approximate the cloud vertical depth using the WV channels. However, the results may insufficiently differentiate between cirrus and convective clouds (Masunaga and Luo, 2016). Our study allows us to cover the cloud development along three dimensions. Compared to the results by Takahashi et al. (2023), we detect a substantially higher number of cloud tracks with at least one DCC. With the ML model, we have the potential to achieve global predictions of the radar reflectivity and reduce the false detection of convective cells.

5.1 Regional influences on the cloud life-cycle

Our results are consistent with measurements from cloud-penetrating aircraft (LeMone and Zipser, 1980) or the analysis of precipitation data (Zipser et al., 2006). Clustered clouds regenerate their convective activity in response to the diurnal forcing of surface heating (Futyan and Genio, 2007). Most MCSs initiate during daytime, which points toward the importance of local surface characteristics for the propagation of convective organisation (Vondou, 2012; Takahashi et al., 2023). With the onset of the WAM, convective systems may sustain through the night as the nocturnal surface cooling is reduced for clustered clouds (Futyan and Genio, 2007). The diurnal cycle of free-tropospheric relative humidity maximises at night over the tropical oceans and alters convective activity. While a higher relative humidity reduces the entrainment into convective plumes, it allows convective air parcels to maintain their buoyancy longer as they rise, producing deeper convective towers (Wall et al., 2020). For instance, our results suggest a connection between the seasonal cycle of convection and the surface type. Convective storms develop during the rainy season in the mountainous highlands and move into the basin at night when katabatic flow prevails (Nicholson, 2018). Within the AOI, convective activity frequently occurs. Developing clouds may travel large distances due to a contiguous advection towards the Atlantic Ocean. However, quantifying the impact of local topography requires further research. Thermal contrasts and diurnal circulation patterns drive the land-ocean differences (Li et al., 2021). We emphasise that the interaction between DCCs affects the life-cycle of clustered convection substantially. A prolonged lifetime may induce a repeated vertical updraft and area growth. Following the results by Takahashi et al. (2017) and Taylor et al. (2022), we observe more intense DCCs and increased growth of the cloud core and anvil for continental convection (Section 4.2.2). At the edges of the AOI, extratropical effects may come into play and affect the cloud life-cycle (Jones et al., 2024). Disentangling the impact of convective processes within the tropics and mid-latitudes remains a challenge and requires an extensive AOI.

5.2 Limitations and future challenges

The input data for the ML model originate from the CloudSat satellite, which lacks sensitivity to observe ice clouds due to an underestimation of the topmost outflow height (Wang et al., 2014). Our results show this limitation in terms of a weak representation of shallow convection and cirrus clouds. Recently released instruments like the flexible combined imager (Holmlund et al., 2021) aboard the Meteosat Third Generation (MTG) satellite system or the spatio-temporal enhanced CPR of the Earth Cloud Aerosol and Radiation Explorer (EarthCARE) mission (Eisinger et al., 2024) have a higher spatial and temporal resolution. The data may allow for a more accurate detection of clustered MCSs and small-scale changes during their life-cycle. In the current study, we did not examine some presumably important influences like the effect of aerosols, the vertical wind shear, or the entrainment rate (Masunaga and Luo, 2016). Including these factors may help to further understand the drivers of convective organisation. We chose the *tobac* framework to detect isolated and clustered convective clouds (Sokolowsky et al., 2024). Nevertheless, we note that no universal detection algorithm exists (Lakshmanan and Kain, 2010). Instead, every algorithm has specific benefits and limitations depending on the use case and study area (Prein et al., 2024). Despite our ability to achieve an approximation of the vertical updraft by the radar reflectivity, it cannot replace a calculation of vertical wind shear (Luo et al., 2008). Although the effect of vertical shear within the tropics is expected to be minor compared to the mid-latitudes, its quantification requires further analysis (Takahashi et al., 2017). Moreover, investigating precipitation patterns associated with clustered convection could lead to a more accurate forecast of extreme events (Kukulies et al., 2021). However, further research is required to sufficiently assess the present and future risks associated with MCSs (Atiah et al., 2023).

6 Conclusions

This study analysed the life-cycle of convective clouds and their deep convective cores over West Africa. Using an ML-based extrapolation of radar reflectivities, we could detect and track convective clouds in 3D throughout all stages of the cloud life-cycle. Compared to using data from a single sensor, our perspective allows a simultaneous coverage of cloud development in the horizontal and vertical dimensions. Tropical convection appears more intense over land than over the ocean. Over continental Africa, we find more long-lasting clouds with multiple deep convective cores. Within these clouds, core interactions impact the intensity and lifetime of the cloud cluster and its life-cycle. Overall, we detect substantial seasonal differences for clouds over both surface types. Convective activity increases in summer, particularly for clustered clouds over the ocean. However, changes in the cloud life-cycle, like the anvil area growth, remain stronger over land during the whole period. With a higher degree of organisation, the interaction of adjacent cores may drive a renewal of convective activity. This leads to a a prolonged cloud life-cycle and a later occurring maximum number of DCCs. Isolated convective cells have a higher cooling and more extensive vertical growth than clustered clouds. Nonetheless, they persist predominately for a short time and show weaker convective activity than clustered systems. In this work, we use the number of convective cores as a single proxy for convective organisation. However, it may be worth comparing these results to a quantification of organisation using more advanced metrics, as done in the accompanying manuscript. The analysis shows a high variability and ambiguous results over different surface types, in particular during the summer season. Expanding the analysis by an investigation of spatial patterns of convective organisation may account for current uncertainties induced by a surface type specific seasonality.

Code and data availability. The level 2B-GEOPROF CloudSat data used in this study are available at the CloudSat Data Processing Center at CIRA/Colorado State University and can be retrieved from http://www.CloudSat.cira.colostate.edu/order-data (CloudSat Data Processing Center, 2024). The Meteosat SEVIRI level 1.5 data used in this study is freely and openly available via the EUMETSAT Data Store at https://navigator.eumetsat.int/product/EO-:EUM:DAT:MSG:HRSEVIRI (EUMETSAT Data Services, 2024). The code used in this study will be released upon publication.

Author contributions. S.B and H.T. designed the study. S.B developed the code for the analysis and visualisation. S.B. and H.T. contributed to the analysis and evaluation of cloud tracks and properties. S.B. and H.T. wrote the draft of the paper. All authors have read and agreed to the published version of the manuscript.

Competing interests. The authors declare that they have no conflict of interest.

Acknowledgements. This work was supported by the project “Big Data in Atmospheric Physics (BINARY)”, funded by the Carl Zeiss Foundation (grant P2018-02-003), and the Max Planck Graduate Center with the Johannes Gutenberg University of Mainz (MPGC). We thank EUMETSAT for providing access to the Meteosat SEVIRI imager data and the Cooperative Institute for Research in the Atmosphere, CSU, for providing access to the CloudSat 2B-GEOPROF data.

References

Andrews, P. C., Cook, K. H., and Vizy, E. K.: Mesoscale convective systems in the Congo Basin: seasonality, regionality, and diurnal cycles, Clim. Dyn., 62, 609–630, https://doi.org/10.1007/s00382-023-06903-7, 2024.

Atiah, W. A., Amekudzi, L. K., and Danuor, S. K.: Mesoscale convective systems and contributions to flood cases in Southern West Africa (SWA): A systematic review, Weather and Climate Extremes, 39, 100 551, https://doi.org/10.1016/j.wace.2023.100551, 2023.

Bacmeister, J. T. and Stephens, G. L.: Spatial statistics of likely convective clouds in CloudSat data, J. Geophys. Res. Atmos., 116, https://doi.org/10.1029/2010JD014444, 2011.

Brüning, S., Niebler, S., and Tost, H.: Artificial intelligence (AI)-derived 3D cloud tomography from geostationary 2D satellite data, Atmos. Meas. Tech., 17, 961–978, https://doi.org/10.5194/amt-17-961-2024, 2024.

Chen, P.-J., Chen, W.-T., Wu, C.-M., and Yo, T.-S.: Convective Cloud Regimes From a Classification of Object-Based CloudSat Observations Over Asian-Australian Monsoon Areas, Geophys. Res. Lett., 48, e2021GL092 733, https://doi.org/10.1029/2021GL092733, 2021.

Chen, S. S. and Houze, R. A.: Diurnal variation and life-cycle of deep convective systems over the tropical pacific warm pool, Q. J. R. Meteorol. Soc., 123, 357–388, https://doi.org/10.1002/qj.49712353806, 1997.

CloudSat Data Processing Center: Data Products, CloudSat DPC [data set], https://www.cloudsat.cira.colostate.edu/data-products, accessed: 2024-12-12, 2024.

Crook, J., Klein, C., Folwell, S., Taylor, C. M., Parker, D. J., Stratton, R., and Stein, T.: Assessment of the Representation of West African Storm Lifecycles in Convection-Permitting Simulations, ESS, 6, 818–835, https://doi.org/10.1029/2018EA000491, 2019.

Cui, W., Dong, X., Xi, B., and Feng, Z.: Climatology of Linear Mesoscale Convective System Morphology in the United States Based on the Random-Forests Method, J. Clim., 34, 7257–7276, https://doi.org/10.1175/JCLI-D-20-0862.1, 2021.

Dixon, M. and Wiener, G.: TITAN: Thunderstorm Identification, Tracking, Analysis, and Nowcasting—A Radar-based Methodology, J. Atmos. Oceanic Tech., 10, 785–797, https://doi.org/10.1175/1520-0426(1993)010<0785:TTITAA>2.0.CO;2, 1993.

Eisinger, M., Marnas, F., Wallace, K., Kubota, T., Tomiyama, N., Ohno, Y., Tanaka, T., Tomita, E., Wehr, T., and Bernaerts, D.: The EarthCARE mission: science data processing chain overview, Atmos. Meas. Tech., 17, 839–862, https://doi.org/10.5194/amt-17-839-2024, 2024.

Esmaili, R. B., Tian, Y., Vila, D. A., and Kim, K.-M.: A Lagrangian analysis of cold cloud clusters and their life cycles with satellite observations, J. Geophys. Res. Atmos., 121, 11,723–11,738, https://doi.org/10.1002/2016JD025653, 2016.

EUMETSAT Data Services: High Rate SEVIRI Level 1.5 Image Data - MSG - 0 degree, https://navigator.eumetsat.int/product/EO:EUM:DAT:MSG:HRSEVIRI, accessed: 2024-12-12, 2024.

Feng, Z., Hardin, J., Barnes, H. C., Li, J., Leung, L. R., Varble, A., and Zhang, Z.: PyFLEXTRKR: a flexible feature tracking Python software for convective cloud analysis, Geosci. Model Dev., 16, 2753–2776, https://doi.org/10.5194/gmd-16-2753-2023, 2023.

Fiolleau, T. and Roca, R.: An Algorithm for the Detection and Tracking of Tropical Mesoscale Convective Systems Using Infrared Images From Geostationary Satellite, IEEE Trans. Geosci. Remote. Sens., 51, 4302–4315, https://doi.org/10.1109/TGRS.2012.2227762, 2013.

Futyan, J. M. and Genio, A. D. D.: Deep Convective System Evolution over Africa and the Tropical Atlantic, J. Clim., 20, 5041–5060, https://doi.org/10.1175/JCLI4297.1, 2007.

Gallus, W. A., Snook, N. A., and Johnson, E. V.: Spring and Summer Severe Weather Reports over the Midwest as a Function of Convective Mode: A Preliminary Study, WAF, 23, 101–113, https://doi.org/10.1175/2007WAF2006120.1, 2008.

Ganetis, S. A., Colle, B. A., Yuter, S. E., and Hoban, N. P.: Environmental Conditions Associated with Observed Snowband Structures within Northeast U.S. Winter Storms, Mon. Weather Rev., 146, 3675–3690, https://doi.org/10.1175/MWR-D-18-0054.1, 2018.

Guillaume, A., Kahn, B. H., Yue, Q., Fetzer, E. J., Wong, S., Manipon, G. J., Hua, H., and Wilson, B. D.: Horizontal and Vertical Scaling of Cloud Geometry Inferred from CloudSat Data, JAS, 75, 2187–2197, https://doi.org/10.1175/JAS-D-17-0111.1, 2018.

Haberlie, A. M. and Ashley, W. S.: A Method for Identifying Midlatitude Mesoscale Convective Systems in Radar Mosaics. Part II: Tracking, JAMC, 57, 1599–1621, https://doi.org/10.1175/JAMC-D-17-0294.1, 2018.

Haynes, J. M., L'Ecuyer, T. S., Stephens, G. L., Miller, S. D., Mitrescu, C., Wood, N. B., and Tanelli, S.: Rainfall retrieval over the ocean with spaceborne W-band radar, J. Geophys. Res. Atmos., 114, https://doi.org/10.1029/2008JD009973, 2009.

Heikenfeld, M., Marinescu, P. J., Christensen, M., Watson-Parris, D., Senf, F., van den Heever, S. C., and Stier, P.: tobac 1.2: towards a flexible framework for tracking and analysis of clouds in diverse datasets, Geosci. Model Dev., 12, 4551–4570, https://doi.org/10.5194/gmd-12-4551-2019, 2019.

Holmlund, K., Grandell, J., Schmetz, J., Stuhlmann, R., Bojkov, B., Munro, R., Lekouara, M., Coppens, D., Viticchie, B., August, T., Theodore, B., Watts, P., Dobber, M., Fowler, G., Bojinski, S., Schmid, A., Salonen, K., Tjemkes, S., Aminou, D., and Blythe, P.: Meteosat Third Generation (MTG): Continuation and Innovation of Observations from Geostationary Orbit, BAMS, 102, E990–E1015, https://doi.org/10.1175/BAMS-D-19-0304.1, 2021.

Horner, G. and Gryspeerdt, E.: The evolution of deep convective systems and their associated cirrus outflows, Atmos. Chem. Phys., 23, 14 239–14 253, https://doi.org/10.5194/acp-23-14239-2023, 2023.

Houze, R. A. and Hobbs, P. V.: Organization and Structure of Precipitating Cloud Systems, Adv. Geophys., 24, 225–315, https://doi.org/10.1016/S0065-2687(08)60521-X, 1982.

Houze Jr., R. A.: Mesoscale convective systems, Rev. Geophys., 42, RG4003, https://doi.org/10.1029/2004RG000150, 2004.

Igel, M. R., Drager, A. J., and van den Heever, S. C.: A CloudSat Cloud-Object Partitioning Technique and Assessment and Integration of Deep Convective Anvil Sensitivities to Sea Surface Temperature, J. Geophys. Res. Atmos., 119, 10 515–10 535, https://doi.org/10.1002/2014JD021717, 2014.

Jackson, L. S., Marsham, J. H., Parker, D. J., Finney, D. L., Fitzpatrick, R. G. J., Rowell, D. P., Stratton, R. A., and Tucker, S.: The Effect of Explicit Convection on Climate Change in the West African Monsoon and Central West African Sahel Rainfall, J. Clim., 35, 1537–1557, https://doi.org/10.1175/JCLI-D-21-0258.1, 2022.

Jones, W., Christensen, M., and Stier, P.: A semi-Lagrangian method for detecting and tracking deep convective clouds in geostationary satellite observations, Atmos. Meas. Tech., 16, 1043–1059, https://doi.org/10.5194/amt-16-1043-2023, 2023.

Jones, W., Stengel, M., and Stier, P.: A Lagrangian perspective on the lifecycle and cloud radiative effect of deep convective clouds over Africa, Atmos. Chem. Phys., 24, 5165–5180, https://doi.org/10.5194/acp-24-5165-2024, 2024.

Kniffka, A., Knippertz, P., and Fink, A. H.: The role of low-level clouds in the West African monsoon system, Atmos. Chem. Phys., 19, 1623–1647, https://doi.org/10.5194/acp-19-1623-2019, 2019.

Kukulies, J., Chen, D., and Curio, J.: The Role of Mesoscale Convective Systems in Precipitation in the Tibetan Plateau Region, J. Geophys. Res. Atmos., 126, e2021JD035 279, https://doi.org/10.1029/2021JD035279, 2021.

Lakshmanan, V. and Kain, J. S.: A Gaussian Mixture Model Approach to Forecast Verification, WAF, 25, 908–920, https://doi.org/10.1175/2010WAF2222355.1, 2010.

LeMone, M. A. and Zipser, E. J.: Cumulonimbus Vertical Velocity Events in GATE. Part I: Diameter, Intensity and Mass Flux, JAS, 37, 2444–2457, https://doi.org/10.1175/1520-0469(1980)037<2444:CVVEIG>2.0.CO;2, 1980.

Li, W., Zhang, F., Yu, Y., Iwabuchi, H., Shen, Z., Wang, G., and Zhang, Y.: The semi-diurnal cycle of deep convective systems over Eastern China and its surrounding seas in summer based on an automatic tracking algorithm, Clim. Dyn., 56, 357–379, https://doi.org/10.1007/s00382-020-05474-1, 2021.

Luo, Z., Liu, G. Y., and Stephens, G. L.: CloudSat adding new insight into tropical penetrating convection, Geophys. Res. Lett., 35, https://doi.org/10.1029/2008GL035330, 2008.

Marchand, R., Mace, G. G., Ackerman, T., and Stephens, G.: Hydrometeor Detection Using Cloudsat—An Earth-Orbiting 94-GHz Cloud Radar, J. Atmos. Oceanic Tech., 25, 519–533, https://doi.org/10.1175/2007JTECHA1006.1, 2008.

Masunaga, H. and Luo, Z. J.: Convective and large-scale mass flux profiles over tropical oceans determined from synergistic analysis of a suite of satellite observations, J. Geophys. Res. Atmos., 121, 7958–7974, https://doi.org/10.1002/2016JD024753, 2016.

Mecikalski, J. R., MacKenzie, W. M., Koenig, M., and Muller, S.: Cloud-Top Properties of Growing Cumulus prior to Convective Initiation as Measured by Meteosat Second Generation. Part I: Infrared Fields, JAMC, 49, 521–534, https://doi.org/10.1175/2009JAMC2344.1, 2010.

Meyer, F.: Topographic distance and watershed lines, Signal Process., 38, 113–125, https://doi.org/10.1016/0165-1684(94)90060-4, 1994.

Nicholson, S. E.: The ITCZ and the Seasonal Cycle over Equatorial Africa, BAMS, 99, 337–348, https://doi.org/10.1175/BAMS-D-16-0287.1, 2018.

Oreopoulos, L., Cho, N., and Lee, D.: New insights about cloud vertical structure from CloudSat and CALIPSO observations, J. Geophys. Res. Atmos., 122, 9280–9300, https://doi.org/10.1002/2017JD026629, 2017.

Orlanski, I.: A Rational Subdivision of Scales for Atmospheric Processes, BAMS, 56, 527–530, https://www.jstor.org/stable/26216020, 1975.

Patra, S. and Kalapureddy, M.: Cloud radar observations of multi-scale variability of cloud vertical structure associated with Indian summer monsoon over a tropical location, Clim. Dyn., 56, https://doi.org/10.1007/s00382-020-05520-y, 2021.

Prein, A. F., Feng, Z., Fiolleau, T., Moon, Z. L., Núñez Ocasio, K. M., Kukulies, J., Roca, R., Varble, A. C., Rehbein, A., Liu, C., Ikeda, K., Mu, Y., and Rasmussen, R. M.: Km-Scale Simulations of Mesoscale Convective Systems Over South America—A Feature Tracker Intercomparison, J. Geophys. Res. Atmos., 129, e2023JD040 254, https://doi.org/10.1029/2023JD040254, 2024.

Raut, B. A., Jackson, R., Picel, M., Collis, S. M., Bergemann, M., and Jakob, C.: An Adaptive Tracking Algorithm for Convection in Simulated and Remote Sensing Data, JAMC, 60, 513–526, https://doi.org/10.1175/JAMC-D-20-0119.1, 2021.

Roca, R., Bergès, J.-C., Brogniez, H., Capderou, M., Chambon, P., Chomette, O., Cloché, S., Fiolleau, T., Jobard, I., Lémond, J., Ly, M., and Picon, L.: On the water and energy cycles in the Tropics, CR GEOSCI, 342, 390–402, https://doi.org/10.1016/j.crte.2010.01.003, 2010.

Ronneberger, O., Fischer, P., and Brox, T.: U-Net: Convolutional Networks for Biomedical Image Segmentation, in: Medical Image Computing and Computer-Assisted Intervention – MICCAI 2015, edited by Navab, N., Hornegger, J., Wells, W. M., and Frangi, A. F., vol. 9351, pp. 234–241, Springer International Publishing, Cham, 2015.

Sassen, K. and Wang, Z.: Classifying clouds around the globe with the CloudSat radar: 1-year of results, Geophys. Res. Lett., 35, https://doi.org/10.1029/2007GL032591, 2008.

Schmetz, J., Pili, P., Tjemkes, S., Just, D., Kerkmann, J., Rota, S., and Ratier, A.: An introduction to Metetsat second generation (MSG), BAMS, 83, 977–992, https://doi.org/10.1175/1520-0477(2002)083<0977:AITMSG>2.3.CO;2, 2002.

Semie, A. G. and Bony, S.: Relationship Between Precipitation Extremes and Convective Organization Inferred From Satellite Observations, Geophys. Res. Lett., 47, e2019GL086 927, https://doi.org/10.1029/2019GL086927, 2020.

Sokolowsky, G. A., Freeman, S. W., Jones, W. K., Kukulies, J., Senf, F., Marinescu, P. J., Heikenfeld, M., Brunner, K. N., Bruning, E. C., Collis, S. M., Jackson, R. C., Leung, G. R., Pfeifer, N., Raut, B. A., Saleeby, S. M., Stier, P., and van den Heever, S. C.: *tobac* v1.5:

introducing fast 3D tracking, splits and mergers, and other enhancements for identifying and analysing meteorological phenomena, Geosci. Model Dev., 17, 5309–5330, https://doi.org/10.5194/gmd-17-5309-2024, 2024.

Steiner, M., Houze, R. A., and Yuter, S. E.: Climatological Characterization of Three-Dimensional Storm Structure from Operational Radar and Rain Gauge Data, JAMC, 34, 1978–2007, https://doi.org/10.1175/1520-0450(1995)034<1978:CCOTDS>2.0.CO;2, 1995.

Stephens, G. L., Vane, D. G., Tanelli, S., Im, E., Durden, S., Rokey, M., Reinke, D., Partain, P., Mace, G. G., Austin, R., L'Ecuyer, T., Haynes, J., Lebsock, M., Suzuki, K., Waliser, D., Wu, D., Kay, J., Gettelman, A., Wang, Z., and Marchand, R.: CloudSat mission: Performance and early science after the first year of operation, J. Geophys. Res. Atmos., 113, https://doi.org/10.1029/2008JD009982, 2008.

Takahashi, H., Luo, Z. J., and Stephens, G. L.: Level of neutral buoyancy, deep convective outflow, and convective core: New perspectives based on 5 years of CloudSat data, J. Geophys. Res. Atmos., 122, 2958–2969, https://doi.org/10.1002/2016JD025969, 2017.

Takahashi, H., Luo, Z. J., Stephens, G., and Mulholland, J. P.: Revisiting the Land-Ocean Contrasts in Deep Convective Cloud Intensity Using Global Satellite Observations, Geophys. Res. Lett., 50, e2022GL102 089, https://doi.org/10.1029/2022GL102089, 2023.

Taylor, C. M., Klein, C., Dione, C., Parker, D. J., Marsham, J., Diop, C. A., Fletcher, J., Chaibou, A. A. S., Nafissa, D. B., Semeena, V. S., Cole, S. J., and Anderson, S. R.: Nowcasting tracks of severe convective storms in West Africa from observations of land surface state, Environ. Res. Lett., 17, 034 016, https://doi.org/10.1088/1748-9326/ac536d, 2022.

Taylor, S., Stier, P., White, B., Finkensieper, S., and Stengel, M.: Evaluating the diurnal cycle in cloud top temperature from SEVIRI, Atmos. Chem. Phys., 17, 7035–7053, https://doi.org/10.5194/acp-17-7035-2017, 2017.

Tomkins, L. M., Yuter, S. E., and Miller, M. A.: Dual adaptive differential threshold method for automated detection of faint and strong echo features in radar observations of winter storms, Atmos. Meas. Tech., 17, 3377–3399, https://doi.org/10.5194/amt-17-3377-2024, 2024.

Vondou, D. A.: Spatio-Temporal Variability of Western Central African Convection from Infrared Observations, Atmos., 3, 377–399, https://doi.org/10.3390/atmos3030377, 2012.

Wall, C. J., Norris, J. R., Gasparini, B., Smith, W. L., Thieman, M. M., and Sourdeval, O.: Observational Evidence that Radiative Heating Modifies the Life Cycle of Tropical Anvil Clouds, J. Clim., 33, 8621–8640, https://doi.org/10.1175/JCLI-D-20-0204.1, 2020.

Wang, X., Cui, C., Cui, W., and Shi, Y.: Modes of mesoscale convective system organization during Meiyu season over the Yangtze River basin, Acta Meteorol. Sin., 28, 111–126, https://doi.org/10.1007/s13351-014-0108-4, 2014.

Yuter, S. E., Houze, R. A., Smith, E. A., Wilheit, T. T., and Zipser, E.: Physical Characterization of Tropical Oceanic Convection Observed in KWAJEX, J. Appl. Meteorol., 44, 385–415, https://www.jstor.org/stable/26185647, 2005.

Zipser, E. J. and LeMone, M. A.: Cumulonimbus Vertical Velocity Events in GATE. Part II: Synthesis and Model Core Structure, JAS, 37, 2458–2469, https://doi.org/10.1175/1520-0469(1980)037<2458:CVVEIG>2.0.CO;2, 1980.

Zipser, E. J., Cecil, D. J., Liu, C., Nesbitt, S. W., and Yorty, D. P.: Where are the most intense thunderstorms on earth?, BAMS, 87, 1057–1072, https://doi.org/10.1175/BAMS-87-8-1057, 2006.